The ER Thioredoxin-Related Transmembrane Protein TMX2 Controls Redox-Mediated Tethering of ER-Mitochondria Contacts (ERMCS)

Junsheng Chen[1], Megan C. Yap[1], Arthur Bassot[1,2], Danielle M. Pascual[3,4], Tadashi Makio[1], Jannik Zimmermann[5], Heather Mast[6], Rakesh Bhat[7], Samuel G. Fleury[1], Yuxiang Fan[1,8], Adriana Zardini Buzatto[9], Jack Moore[10], Klaus Ballanyi[11], Liang Li[9], Michael Overduin[12], M. Joanne Lemieux[12,13], Hélène Lemieux[6], Wen-Hann Tan[14,15], Grazia M.S. Mancini[16], Bruce Morgan[5], Paul C. Marcogliese[3,4,17], and Thomas Simmen[1, 18]

[1] Department of Cell Biology, Faculty of Medicine and Dentistry, Edmonton, AB T6G 2H7, Canada.

[2] Present address: Department of CITI, Team GLIMMER Of lIght, Cancer Research Centre of Lyon - CRCL, INSERM U1052, CNRS UMR 5286, Lyon, France.

[3] Department of Biochemistry and Medical Genetics, Rady Faculty of Health Sciences, University of Manitoba, Winnipeg, Manitoba, Canada.

[4] Children's Hospital Research Institute of Manitoba (CHRIM), University of Manitoba, Winnipeg, Manitoba.

[5] Zentrum für Human- und Molekularbiologie (ZHMB), Universität des Saarlandes, Biochemie Campus, Geb. B2.2, D-66123, Saarbrücken, Germany.

[6] Faculty Saint-Jean, Department of Medicine, Faculty of Medicine and Dentistry, Edmonton, AB T6G2H7, Canada.

[7] Precision Biolaboratories, St. Albert, AB T8N 5A7, Canada.

[8] Present address: Department of Neurosurgery, Xuanwu Hospital, Capital Medical University, Beijing, 10053, China.

[9] Department of Chemistry, University of Alberta, Edmonton, Alberta, Canada.

[10] Alberta Proteomics and Mass Spectrometry Facility, University of Alberta, 4096 Katz Research Building, Edmonton AB T6G2E1, Canada.

[11] Department of Physiology, University of Alberta, Edmonton, AB T6G2H7, Canada.

[12] Department of Biochemistry, University of Alberta, Edmonton, Alberta T6G 2H7, Canada.

[13] Li Ka Shing Institute of Virology, University of Alberta, Edmonton, Alberta T6G 2E1, Canada.

[14] Harvard Medical School, Boston, MA, USA.

[15] Division of Genetics and Genomics, Boston Children's Hospital, Boston, MA, 02115, USA.

[16] Department of Clinical Genetics, Erasmus University Medical Center, PO Box 2040, 3000 CA Rotterdam, the Netherlands.

[17] Excellence in Neurodevelopment and Rehabilitation Research in Child Health (ENRRICH) Theme, Winnipeg, Manitoba.

[18] Corresponding author and lead contact:

Tel: (780) 492-1546

Email: Thomas.Simmen@ualberta.ca

Summary

Thioredoxin-related transmembrane proteins (TMX) of the endoplasmic reticulum (ER) have emerged as key regulators of ER membrane properties. Within the ER lumen, TMX proteins and other ER redox enzymes determine oxidative conditions, which control the formation of ER-mitochondria membrane contacts (ERMCS) and determine their function. ERMCS exhibit cytoplasmic redox nanodomains, derived from ER and mitochondrial reactive oxygen species (ROS), whose mechanistic regulation is uncharacterized. Our research has identified the ER protein TMX2, which uses its unique cytosolic thioredoxin domain to prevent cytosolic sulfenylation of mitochondrial outer membrane proteins such as TOM70 through a functional interaction with peroxiredoxin-1 (PRDX1). By doing so, TMX2 interferes with the TOM70 ERMCS tethering function and reduces mitochondrial Ca^{2+} flux and metabolism. Recently, TMX2 mutations have been identified to cause a neurodevelopmental disorder with microcephaly, cortical malformations, and spasticity (NEDMCMS). Using TMX2-mutated NEDMCMS patient cells, we demonstrate that compromising TMX2 through mutation reproduces mitochondrial defects. In a fly *in vivo* model, TMX2 knockdown manifests predominantly in glial cells. Our results therefore provide important mechanistic insight into NEDMCMS and mechanistically link TMX2-mediated control of ERMCS to brain development and function.

Graphical Abstract

The transmembrane thioredoxin-related TMX2 prevents TOM70 sulfenylation at ERMCS, thus maintaining normal mitochondria metabolism in wild-type cells. TMX2 knockout leads to TOM70 sulfenylation and tight ERMCS formation. This then increases ROS production, unbalances mitochondrial lipids, and relatively shifts OXPHOS electron supply to complex II.

Keywords

Endoplasmic reticulum (ER), mitochondria, redox, reactive oxygen species (ROS), Ca^{2+}, TMX2, peroxiredoxin (PRDX), TOM70

63 **Introduction**

64

65 The membranes of the endoplasmic reticulum (ER) contain thioredoxin-related transmembrane
66 proteins (TMX) (Guerra & Molinari, 2020), which can communicate the status of the ER to adjacent
67 organelles, including the transmission of ER stress at the nuclear envelope (Kucinska et al., 2023) or at
68 ER-mitochondria contacts (ERMCS) (Raturi et al., 2016). Importantly, reactive oxygen species (ROS)
69 control ERMCS, reflected in their rich content of multiple ROS producers (Yoboue et al., 2018). This
70 accumulation of H_2O_2 can originate from within the ER (Gorin et al., 2003) or from mitochondria
71 (Sharma et al., 2011). An important H_2O_2-mediated mechanism operating at ERMCS is based on the
72 multipass transmembrane NADPH oxidase 4 (NOX4), which promotes ER membrane protein oxidation
73 (Beretta et al., 2020), and increases ERMCS Ca^{2+} flux to activate mitochondria (Booth et al., 2021).
74 Similarly, ER oxidoreductin 1 (ERO1) localizes to ERMCS (Gilady et al., 2010), where it produces H_2O_2
75 during the early phases of ER stress. This activity leads to the lumenal oxidation and oligomerization of
76 the UPR sensor protein PERK, increases ERMCS formation, and activates mitochondria (Bassot et al.,
77 2023). These findings suggest that the amount of ROS at ERMCS may determine their function but could
78 also dictate the proportion of tight (<10 nm membrane distance) versus wide ERMCS spacing (>30 nm
79 membrane distance). Such a switch of ERMCS spacing could hypothetically favor lipid or Ca^{2+} signaling,
80 respectively (Giacomello & Pellegrini, 2016).

81 In contrast to ER lumenal redox control of ERMCS, no cytosolic oxidase or reductase activity has
82 been associated with this structure. In principle, enzymes of the peroxiredoxin family could control
83 cytosolic redox at ERMCS, since they are highly efficient at reducing H_2O_2 levels through their
84 peroxidatic and resolving cysteines (Rhee, 2016). This activity extends to the periphery of mitochondria,
85 since peroxiredoxin-1 (PRDX1), a member of the 2-cysteine peroxiredoxin family, absorbs
86 mitochondrial H_2O_2 output (Hoehne et al., 2022). Once oxidized, cytosolic thioredoxins reduce PRDXs
87 (Pannala & Dash, 2015). Alternatively, 2-cysteine PRDXs can oxidize substrates in a redox relay, such
88 as towards ASK1 in the case of PRDX1 (Jarvis et al., 2012). The synthesis of these redox reactions can
89 lead to sharp H_2O_2 gradients near sources of ROS, generating a localized, PRDX-controlled ROS
90 floodgate (Wood et al., 2003). However, not many cytosolic ERMCS oxidation targets are currently
91 known. One candidate is the ERMCS tether Mitofusin-2. This GTPase undergoes oxidation-dependent
92 changes of function in mitochondrial dynamics, but whether this affects ERMCS is not clear (Shutt et
93 al., 2012, Thaher et al., 2018).

94 To address this knowledge gap, we have focused on TMX2. This member of the TMX family has a

95 cytosolic thioredoxin domain containing a SNDC motif (Guerra & Molinari, 2020). TMX2 mutations
96 have been linked to a neurodevelopmental disorder with microcephaly, cortical malformations, and
97 spasticity (NEDMCMS) (Ghosh et al., 2020, Vandervore et al., 2019). TMX2 can interact with ERMCS
98 proteins like calnexin (Vandervore et al., 2019), but it is thought to lack a significant lumenal domain
99 (Oguro & Imaoka, 2019). We therefore searched for interactors that could be targets on the cytosolic
100 ERMCS face. Accordingly, we found that TMX2 modulates the redox state of mitochondrial TOM70
101 (translocase of the outer membrane 70). TOM70 not only promotes mitochondrial protein import, but
102 can also tether the ER to mitochondria through interaction with IP_3Rs (Filadi et al., 2018). Through its
103 reductive activity, TMX2 prevents TOM70 sulfenylation and promotes redox-controlled ERMCS
104 spacing, thereby interfering with ERMCS metabolic signaling. Our results describing the activity of
105 TMX2 and its contributions for ERMCS functions provide important insight into NEDMCMS
106 (Vandervore et al., 2019). Our fly *TMX2* knock-down animal model not only reproduces the NEDMCMS
107 phenotype but also identifies glial cells as the point of origin of the pathology.
108
109 **Results**
110
111 **TMX2 is a polytopic ERMCS transmembrane protein with a cytosolic SXXC motif**
112 To address the mechanistic basis for NEDMCMS, we revisited the TMX2 topology and localization
113 to determine where its putative catalytic domain might interact with substrates. From an AlphaFold three-
114 dimensional structure model (Jumper et al., 2021), we determined that TMX2 likely exhibits four
115 transmembrane domains across the ER membrane. These are preceded by an N-terminal membrane-
116 apposed α-helix and followed by a cytosolic C-terminal thioredoxin domain (Figure 1A) containing a
117 conserved $SXXC_{170}$ motif (Figure 1B). As expected from the absence of potential glycosylation sites in
118 the short lumenal domain, TMX2 is not glycosylated (Supplemental Figure 1A).
119 Next, we investigated this postulated topology biochemically by proteinase K digestion and
120 expressed TMX2 with a Flag-tag after the first transmembrane domain in the ER lumen (position 49;
121 version 1) or a Flag-tag at the N-terminus (position 1; version 2) in HEK293 cells. Version 1 yielded a
122 stable Flag-tagged 16 kDa fragment, corresponding to a Flag-tagged fragment with protected
123 transmembrane and lumenal domains extending from proline 24 to methionine 125, with the short
124 cytosolic domain from arginine 81 to histidine 86 (RSITV) likely embedded into the membrane (Figure
125 1C). In contrast, version 2 with the cytosolically exposed Flag tag, as well as the signal from an anti-
126 TMX2 antibody directed towards the cytosolic domain were fully degraded (Figure 1C). Artificial

127 glycosylation sites at residues 49 (L49N, projected lumenal), 71 (F71N, projected TM #2), N80 (R82T,
128 projected TM #2), and N92 (F94S, projected TM #3, see Supplemental Figure 1B) all failed to generate
129 glycosylated TMX2, in contrast to ERO1α used as a positive control (Supplemental Figure 1B).
130 Therefore, TMX2 is a fully embedded four-transmembrane protein whose biggest extension corresponds
131 to a cytosolic thioredoxin domain that is equipped with a classic KKXX ER retrieval motif at the C-
132 terminus (Figure 1D).
133 Based on its co-fractionation with ERMCS markers VDAC1 and TMX1 on an Optiprep ER gradient
134 (Lynes et al., 2012), we hypothesized that TMX2 is an ERMCS protein. Confirming this, we detected
135 overlap between mitochondrial TOM70 and a validated anti-TMX2 antiserum in U251 MG cells (Figure
136 1D). A similar pattern was observed for the 3D reconstruction of co-localization between transfected
137 Flag-tagged TMX2 and ERp57 or mitochondria in HeLa cells (Supplemental Figure 1C). Next, we
138 quantitatively assayed TMX2 localization with a Percoll fractionation protocol that isolates
139 mitochondria-associated membranes (MAMs) from the remainder of the ER. This showed that TMX2 is
140 highly enriched in the MAM fraction, similar to calnexin, in both U251 MG (Figure 1E) and HeLa cells
141 (Supplemental Figure 1D). ER and mitochondria association of TMX2 was not responsive to changes in
142 redox conditions (Supplemental Figure 1E). To test whether TMX2 plays a role in ERMCS tethering, we
143 next tested whether it is preferentially associated with tight (<10 nm) or widely spaced (>30 nm) ERMCS
144 (Giacomello & Pellegrini, 2016). Thus, we quantified co-localization of endogenous TMX2 with SPLICS
145 sensor proteins (Cieri et al., 2018), which specifically detect tight or wide ERMCS, respectively
146 ($SPLICS_{short}$ or $SPLICS_{long}$, Figure 1F). This showed that TMX2 predominantly localizes to wide
147 ERMCS. Next, we knocked out TMX2 in U251 MG cells by CRISPR/Cas9 (Supplemental Figure 1F).
148 Transmission electron microscopy of these cells showed that TMX2 knockout increased the number of
149 tight ERMCS, while it approximately halved the number of widely spaced ERMCS (Figure 1G). This
150 was reproduced in U251 MG cells transfected with TMX2 RNAi (Supplemental Figure 1G, H). Together,
151 our analyses showed that TMX2 provides a thioredoxin domain on the cytoplasmic face of widely spaced
152 ERMCS.
153
154 **TMX2 Interacts with TOM70 to Decrease ERMCS Tethering**
155 To further investigate the role of TMX2 for ERMCS, we used an unbiased mass-spectrometric
156 approach to characterize the TMX2 interactome. Our crosslinked mass spectrometry (CLMS) showed
157 that Flag-TMX2 interactors are found within a variety of functional clusters (Supplemental Figure 2A).
158 Within this interactome, we were able to generate a protein-protein interaction network amongst multiple

159 mitochondrial outer membrane (OMM) proteins that mediate ERMCS tethering and its regulation (Figure
160 2A), including members of the voltage-dependent anion channels (VDAC) (Reina et al., 2020, Shoshan-
161 Barmatz et al., 2018), and TOM70 (Filadi et al., 2018).
162 TOM70 is enriched on ERMCS, where it acts to promote tethering (Filadi et al., 2018) and is known
163 to be redox-responsive in yeast (Kreimendahl et al., 2020). This made it a good candidate target for
164 TMX2. We validated their interaction through co-immunoprecipitation of endogenous TOM70 with
165 Flag-tagged TMX2 (in parallel to the known TMX2/calnexin interaction, Figure 2B) and with
166 endogenous TMX2 (Figure 2C). Moreover, it has spatial consequences. While reduction of TMX2 levels
167 increases ERMCS (<10 nm, Figure 1G), ERMCS partially revert to normal upon depletion of both TMX2
168 and TOM70 (Figure 2D, Supplemental Figure 2B).
169 Next, we investigated the requirements of the TOM70-TMX2 interaction. This analysis showed that
170 mutation of C170, the sole cysteine within the TMX2 active site, abrogated co-immunoprecipitation
171 (Figure 2E). This dependence on C170 was also observed for calnexin but not for VDAC1 (Supplemental
172 Figure 2C). We further investigated whether ERMCS spacing depends on TMX2 by showing that
173 plasmid-based over-expression of wildtype TMX2 (Supplemental Figure 2D) increased ERMCS
174 spacing, manifesting as a more than 30% reduction of tight ERMCS upon over-expression (Figure 2F).
175 Importantly, this change did not occur with the C170S mutant, thus demonstrating that a cytosolic
176 thioredoxin domain is instrumental in the ability of TMX2 to increase ERMCS spacing in a TOM70-
177 dependent manner.
178
179 **TMX2 Prevents TOM70 Sulfenylation with the Help of PRDX1**
180 To understand the consequence of TMX2 for ERMCS, we characterized the TMX2-TOM70
181 interaction and its function. Given the large size of the cytosolic domain of TOM70, we constructed
182 deletion mutants of the chaperone-binding (residues 138-251) and substrate-binding (residues 468-608)
183 domains. Deletion proteins of the core domain (residues 292-468) were poorly expressed and showed
184 drastically altered mitochondrial structure (Supplemental Figure 3A). In contrast, deletion mutants of the
185 chaperone-binding domain were well expressed but did not allow for TMX2 interaction (Supplemental
186 Figure 3B). Interestingly, the cysteine-rich chaperone-binding domain was previously identified as
187 critical to prevent mitochondrial stress in yeast (Backes et al., 2021), suggesting TMX2 affects the
188 functions of TOM70 in ERMCS tethering or mitochondrial protein import.
189 Unlike their typically oxidizing ER-lumenal counterparts, cytosolic thioredoxin proteins can directly
190 prevent protein oxidation (Arner & Holmgren, 2000) or promote PRDX antioxidant functions (Netto &

191 Antunes, 2016). To investigate whether TMX2 fits into the ER lumenal or cytosolic thioredoxin type,
192 we first used a redox-sensitive GFP (ro-GFP2)-based assay as a qualitative readout for TMX2 activity.
193 Genetic fusion constructs between roGFP2 and thioredoxin superfamily proteins have previously been
194 used to study structure-function relationships in both PRDXs and glutaredoxins (Liedgens et al., 2020,
195 Staudacher et al., 2018, Zimmermann et al., 2021). Expressing a roGFP2-TMX2$_{cytosolic}$ construct in
196 specifically engineered yeast cells, TMX2 neither showed a thiol peroxidase-like nor a glutaredoxin-like
197 activity, in contrast to human glutaredoxin-1 (Supplemental Figure 3C).
198 To determine whether the TMX2-TOM70 interaction could instead prevent oxidation of TOM70,
199 we turned to the DCP-Bio1 compound, a reagent that specifically detects sulfenylated cysteines (Poole
200 et al., 2007) (Figure 3A). We detected threefold increased DCP-Bio1-labeled TOM70 signals in siTMX2-
201 transfected HEK293 cells (Figure 3B). This was confirmed by mass-spectrometric analysis that detected
202 C206 sulfenylation (Figure 3C). The oxidation of TOM70 in TMX2 knock-down cells required ROS
203 production in mitochondria and the ER from OXPHOS complex III and NOX4 (Supplemental Figure
204 3D). To distinguish between a passive oxidation or oxidation involving PRDXs, we tested whether
205 TMX2 can interact with cytosolic PRDX. Indeed, through CLMS, we could detect PRDXs 1, 2 and 6
206 within the TMX2 interactome (Figure 3D). This interaction was confirmed by co-immunoprecipitation
207 for PRDX1 (Figure 3E).
208 Next, we tested whether PRDXs functionally interact with TMX2 to prevent TOM70 sulfenylation.
209 Consistent with such an activity, we found TOM70 sulfenylation increased upon PRDX1 and PRDX2,
210 but not PRDX6 knock-down (Figure 3F). If TMX2 uses PRDX1 and PRDX2 to prevent TOM70
211 sulfenylation, their binding to TOM70 should increase in the absence of TMX2. We therefore screened
212 the TOM70 interactome of TMX2 wild-type and KO U251 MG cells for interacting PRDXs and detected
213 PRDX1 bound to TOM70 in KO cells (Figure 3G). Increased interaction between TOM70 and PRDX1
214 was also detected in KO over wild-type cells by co-immunoprecipitation (Figure 3H). This interaction
215 was prevented by the transfection of wild-type TMX2 but not by C170S TMX2 (Figure 3I). For PRDX2,
216 we could only detect minor changes in the interaction pattern. Therefore, TMX2 promotes the PRDX1
217 and PRDX2 antioxidant activities to prevent TOM70 sulfenylation from mitochondrial and ER ROS.
218
219 **TMX2 Decreases the Mitochondrial Ca^{2+} Response**
220 We hypothesized that TMX2-controlled ERMCS spacing impacts this membrane contact not just
221 spatially but also functionally. Therefore, we next analyzed the protein content of ERMCS in U251 MG
222 TMX2 KO cells. We took advantage of a recently published, detailed description of the ERMCS

223 proteome that is based on a split BioID approach (Kwak et al., 2020) and quantified changes of *bona fide*
224 ERMCS proteins within ERMCS isolates from U251 MG TMX2 wild-type and KO cells through LC-
225 MS analysis. We found that most ERMCS proteins (e.g., PDIA6, VAPB, TMX1) increased significantly
226 except for FUNDC2 (Figure 4A) and that, overall, the number of proteins associated with ER protein
227 folding and ER membrane organization increased in parallel (Supplemental Figure 4A), a phenotype
228 known to promote ER-mitochondria Ca^{2+} flux in multiple examples (Simmen & Herrera-Cruz, 2018).
229 Thus, we tested whether this was indeed the case. Our results showed that histamine-triggered Ca^{2+}
230 transfer from the ER to mitochondria increased by about 50% in TMX2 KO (Figure 4B) or knock-down
231 cells (Supplemental Figure 4B). In contrast, over-expression of wildtype TMX2 but not of the C170S
232 mutant decreased Ca^{2+} transfer (Figure 4B). Since we detected changes in Ca^{2+} flux, we next released
233 mitochondrial Ca^{2+} with FCCP that dissipates the mitochondrial membrane potential and blocks store-
234 operated Ca^{2+} entry (Yoast et al., 2021). This was not affected by TMX2 (Figure 4C, Supplemental Figure
235 4C). Consistent with TMX2-controlled Ca^{2+} communication, a proximity ligation assay (PLA) for the
236 TOM70-IP_3R1 interaction pair detected increased signals upon TMX2 knock-down in HeLa cells (Figure
237 4D). These results suggested that TMX2 prevents excessive Ca^{2+} transfer between the ER and
238 mitochondria but does not significantly alter mitochondrial Ca^{2+} content.
239 Such an effect could be based on increased ER Ca^{2+} content or facilitated Ca^{2+} release by TMX2, as
240 reported (Gutierrez et al., 2020, Raturi et al., 2016). While reduced levels of TMX2 did not alter ER Ca^{2+}
241 release dynamics (Supplementary Figure 4D), they reduced ER Ca^{2+} content (Figure 4E, Supplementary
242 Figure 4E). In contrast, TMX2 over-expression increased ER Ca^{2+} content, dependent on the presence of
243 C170 within its thioredoxin domain (Figure 4E). Therefore, TMX2 increases ER Ca^{2+} content and
244 inhibits ER-mitochondria Ca^{2+} transfer.
245
246 **TMX2 Maintains the Mitochondrial Lipidome and Reduces ROS from OXPHOS**
247 ERMCS do not only determine Ca^{2+} signaling, they also control the global cellular lipidome such as
248 phosphatidylcholine (PC) levels (Ganji et al., 2023). For our analysis, we decided to focus on lipid species
249 with known functional connections to ERMCS (Vance, 2020) and analyzed TMX2 U251 MG wildtype
250 and KO cells through LC-MS and LC-MS/MS. In addition to PC, we included phosphatidylserine (PS)
251 that is converted to phosphatidylethanolamine (PE) within mitochondria (Vance, 2015) and phosphatidic
252 acid (PA), which determines the mitochondrial cardiolipin (CL) content (Yeo et al., 2021), all of which
253 are under the control of ERMCS (Perea et al., 2023). This showed that most changes occurred amongst
254 the PC and Hexosylceramide (HexCer) species (Supplemental Figure 5A). When inspecting a lipidome

255 volcano plot, we found that several CL species increased in KO cells (Figure 5A). A more detailed
256 analysis showed that PC and PE species of the ether subtype were decreased (Figure 5B, C), which is
257 known to increase mitochondrial ROS production (Chen et al., 2023).

258 Together, the promoted Ca^{2+} signaling (Cardenas et al., 2010) and the increase of CL (Zhang et al.,
259 2002) predicted that TMX2 KO cells should show increased mitochondrial respiration but at the cost of
260 increased ROS production. Accordingly, we found that TMX2 depletion increased maximal respiration
261 by about 30% (Figure 5D, Supplemental Figure 5B). The inhibition of mitochondrial Ca^{2+} import with
262 Ru265 reversed this increase in full, while TOM70 knock-down partially reduced it (Supplemental
263 Figure 5C). Conversely, TMX2 over-expression reduced maximal respiration by about 20% compared
264 to control cells (Figure 5E). These changes in respiration were accompanied by increased ROS
265 production upon TMX2 depletion (Figure 5F, Supplemental Figure 5D). Conversely, ROS decreased in
266 TMX2 over-expressing cells, but not with C170S (Supplemental Figure 5E). Mitochondrial dysfunction
267 could derive from abnormal ERMCS spacing, or from altered TOM70 oxidation. To distinguish between
268 these possibilities, we first introduced FATE-1 to increase ERMCS spacing. This abolished increased
269 ROS production completely (Figure 5G). Next, we depleted TOM70 in wild-type and TMX2 KO cells.
270 This experiment showed that TOM70 knock-down overall decreased ROS but did not result in a
271 difference between TMX2 wild-type and KO U251 MG cells (Supplemental Figure 5F). Importantly, the
272 ROS observed from TMX2 KO were derived from ER (NOX4) and mitochondrial sources (complex I
273 and III, Figure 5H). These findings indicate that the mitochondrial dysfunction, characterized by altered
274 respiration and increased ROS production, is connected to ERMCS spacing and proper mitochondrial
275 Ca^{2+} homeostasis, functions partially dependent on TOM70.
276

277 **TMX2 Preserves the Mitochondrial Proteome**

278 To test whether TMX2 preserves normal mitochondrial functions through maintenance of the
279 mitochondrial proteome, we biochemically isolated the mitochondria proteome from U251 MG wildtype
280 and TMX2 KO cells and analyzed it by mass spectrometry (Figure 6A). This revealed that several
281 mitochondrial proteins decreased in TMX2 KO cells. A subsequent treatment with proteinase K to
282 eliminate surface proteins revealed significant decreases in OXPHOS (e.g., NDUFB9, and COX5B) and
283 Krebs cycle components (e.g., SUCLG1). These decreases were not uniform (Supplemental Figure 6A),
284 but the decrease in mitochondrial protein content was most significant for proteins of the mitochondrial
285 inner membrane (MIM, Figure 6B). Within the OXPHOS machinery, components of OXPHOS complex
286 IV and V decreased, while OXPHOS complex II showed an increase (Figure 6C). We verified this pattern

287 in total lysates for select mitochondrial proteins and found the expected changes for representative
288 complex I-V proteins (Figure 6D). These changes observed within KO cells could not be reversed by
289 increased ERMCS spacing through FATE-1 (Supplemental Figure 6B). An obvious explanation for these
290 findings could be the known function of TOM70 in mitochondrial protein import. To investigate this
291 question, we took two approaches: 1) we tested whether known TOM70 importome proteins
292 (Morgenstern et al., 2021) show consistently decreased interaction with TOM70 in the absence of TMX2.
293 This showed that some of these proteins like the mitochondrial fission and fusion controlling ARMC10
294 (Chen et al., 2019) indeed interacted less with TOM70 in TMX2 KO cells. However, many others (e.g.,
295 DLAT) did not (Figure 6E). 2) We tested whether the transcription of some of the most changed proteins
296 was altered in TMX2 KO cells. This also did not reveal a trend (Figure 6F), suggesting that TMX2
297 modulates the mitochondrial proteome independent of TOM70.
298 To further examine the bioenergetic role of TMX2, we measured the mitochondrial membrane
299 potential and found it was lower upon TMX2 depletion (Supplemental Figure 6C). In addition, we
300 detected that AMP-activated protein kinase (AMPK) phosphorylation levels were unchanged in TMX2
301 KO cells (Supplemental Figure 6D), correlating with the inability of TMX2 KO cells to rescue their low
302 ATP levels (Supplemental Figure 6E). Within mitochondria of TMX2 KO cells and to a lesser extent
303 upon TMX2 RNAi transfection, O_2 flux increased most within complex IV and the succinate (S)-pathway
304 (Gnaiger, 2009) (Figure 6G, Supplemental Figure 6F, G). The latter observation correlates with the
305 observed specific increase of complex II proteins (Figure 6C), which accept succinate from the Krebs
306 cycle (Lemieux et al., 2017).
307
308 **TMX2 Patient Mutations and *in vivo* Knock-down Compromise TMX2 Function**
309 Previous reports on TMX2 have suggested that the autosomal-recessive NEDMCMS pathology
310 derives from a loss of function. This is based on *TMX2* truncating variants observed in patients and the
311 reduction of TMX2 protein levels in patient samples (Vandervore et al., 2019). The present study
312 provides the first comprehensive, functional analysis of TMX2. We sought to investigate some of the
313 key functions we have herein identified in *TMX2* variant cells from NEDMCMS patients and *TMX2*
314 knock-down in an animal model to determine the pathogenesis of NEDMCMS. We initiated our
315 characterization with three NEDMCMS patient fibroblasts. These cell lines were labeled P1 (male,
316 transheterozygous D55A/Δ136-296); P4 (male, homozygous G56A), and P5 (female, homozygous
317 G56A) (Vandervore et al., 2019) (Supplemental Figure 7A). TMX2 protein levels were reduced in P1,
318 while they were comparable in P4 and P5 (Figure 7A). We confirmed that the mitochondrial proteins

319 under the control of TMX2 were decreased (e.g., TOM70, SUCLG1). AMPK phosphorylation was
320 increased in P4 and P5, but not P1 (Figure 7A). Therefore, NEDMCMS patient cells partially recapitulate
321 TMX2 depletion results (Figure 6). Regarding the mitochondrial proteins of complexes I-V, this
322 mirroring was also incomplete and was restricted to decreases in complex III UQCRC2 in P4 and P5
323 (Supplemental Figure 7B). We proceeded with a functional characterization of the defects in NEDMCMS
324 patient cells and detected increased ERMCS in P1 but not P4 and P5 (Figure 7B), increases in maximal
325 respiration (Figure 7C), and increases of various extent in cellular ROS (Figure 7D). Unlike the decrease
326 in mitochondrial membrane potential observed upon TMX2 depletion (Supplemental Figure 6E), we
327 detected an increase in P1 and P5, while P4 showed no change (Supplemental Figure 7C), accompanied
328 by an insignificant decrease in total ATP (Supplemental Figure 7D). Therefore, NEDMCMS patient cells
329 do not provide an unequivocal loss of function phenotype but are rather characterized by complex
330 ERMCS dysfunction, where respiration and ROS matched the TMX2 depletion phenotype.

331 Next, we investigated which cell type could compromise nervous system functions in patients. To
332 approach this question, we took advantage of the high degree of conservation observed for TMX2 (Figure
333 1A, B) and chose the *D. melanogaster* fly model. The uncharacterized *Drosophila* gene, *CG11007*, is the
334 single ortholog to human *TMX2* having a high ortholog prediction (DIOPT) score of 16/19 (Hu et al.,
335 2011). Recent single-cell sequencing data from the adult fly brain indicate that *CG11007* is widely
336 expressed in the adult nervous system in both neurons and glia (Davie et al., 2018). To determine the *in*
337 *vivo* consequences of loss of *CG11007*, we used the well-established Gal4/UAS system to selectively
338 reduce *CG11007* mRNA in the nervous system in either all neurons or all glia via RNAi (interference).
339 Pan-neuronal knock-down of *CG11007* using nSyb (neuronal Synaptobrevin)-Gal4 at 25ºC led to viable
340 flies that were grossly normal. Neuronal reduction of *CG11007* did not cause any significant climbing
341 deficits or mechanically-induced seizures in aged (20-day old flies) flies of either sex at this temperature
342 (Supplemental Figure 7E). Conversely, pan-glial knock-down of *CG11007* using repo-Gal4 led to
343 increased time to climb in aged flies of either sex at 25ºC (Figure 7E). Climbing was not significantly
344 different from luciferase RNAi controls in young (5-day old flies). Similarly, glial reduction of *CG11007*
345 at 25ºC causes seizure-like behaviour (freezing and/or spasticity) in aged flies after 15 seconds of vortex
346 (Figure 7F). This bang-sensitivity phenotype was observed in both sexes and while not significant,
347 showed a trend in young flies. Our results indicate that the glial function of CG11007 is important for
348 appropriate neuronal function in the organism.

349 The Gal4/UAS system is temperature-dependent (Nagarkar-Jaiswal et al., 2015) where increased
350 temperature leads to increased Gal4-mediated UAS binding and subsequent RNAi knock-down of the

351 mRNA target. Similar to 25ºC, neuronal knock-down of *CG11007* at 29ºC led to viable flies that showed
352 no climbing deficits or mechanically-induced seizures in aged (20 days old) flies of either sex at this
353 temperature (Supplemental Figure 7G, H). Interestingly, neuronal knock-down of *CG11007* caused a
354 mild but significant increase in climbing speed in aged flies at 29ºC (Supplemental Figure 7H).
355 Regardless, these data indicate that CG11007 is not critical to neuronal function in flies. In contrast, glial
356 knock-down of *CG11007* at 29ºC causes sub-viability as flies no longer eclose from pupae at the expected
357 Mendelian ratios (Supplemental Figure 7I). Adult flies that do survive at 29ºC have significant climbing
358 deficits (Supplemental Figure 7J) and seizure-like behaviour (Supplemental Figure 7K) at 5 days old
359 when compared to luciferase RNAi controls of the same sex. Lastly, glial knock-down of *CG11007* at
360 29ºC significantly shortens fly lifespan (Figure 7G). 50% survival dropped from 28 days to 18 days in
361 males and from 44 days to 40 days in females. Together, these data indicate the importance of glia TMX2
362 and CG11007 in long-term health and nervous system function.
363
364 **Discussion**
365
366 Our previous research had identified ER-lumenal ROS production as critical for the increased
367 formation of ERMCS during ER stress (Bassot et al., 2023). However, the formation of ERMCS redox
368 nanodomains on the cytosolic face of these membrane contacts indicates that this location also undergoes
369 ROS-dependent changes (Booth et al., 2016). With the present study, we have identified the ubiquitous
370 TMX2 protein as key in the control of such changes. We have determined that TMX2 cooperates with
371 PRDX1 and to a lesser extent with PRDX2 to control ERMCS cytosolic redox. This result could be tied
372 to the common cytosolic role of thioredoxins as reductases of PRDXs. Alternatively, TMX2 could simply
373 absorb ROS at ERMCS with the help of PRDXs. Regardless, ER membrane-embedded TMX2 therefore
374 connects the ER environment with the cytosol and its redox enzymes. Subsequently, it directs ER and
375 mitochondrial ROS supply away from mitochondrial surface proteins such as TOM70. In the case of this
376 substrate, TMX2 prevents sulfenylation that normally promotes ERMCS tethering. To do so, TMX2 uses
377 a SNDC motif within its thioredoxin domain. This sequence is rare within mammalian thioredoxins but
378 resembles the one found within the cytosolic E. coli chaperedoxin cnoX (SQHC), which cooperates with
379 heat shock proteins to similarly protect its substrates from permanent oxidation (Dupuy et al., 2023,
380 Goemans et al., 2018).
381 We have therefore identified mitochondrial sulfenylation as a novel signal determining ERMCS
382 spacing: TOM70 sulfenylation correlates with tight ERMCS, while TMX2 prevents this state and

383 promotes wide ERMCS spacing. PRDX1 interaction with TOM70 increases in the former scenario, likely
384 in a futile interaction, but its TOM70 interaction is not detectable in the latter. This indicates that PRDX1
385 normally eliminates ROS that can otherwise sulfenylate TOM70 in the absence of TMX2. While we used
386 TOM70 as a model substrate in this study, multiple mitochondrial surface proteins are under redox
387 control. Some of these, including VDAC1, are amongst the TMX2 interactome, although in a C170-
388 independent manner. Whether their oxidation state (Reina et al., 2020) plays a role for VDAC-controlled
389 ERMCS functions (Prasad et al., 2015) is unclear.

390 The consequences of TMX2-mediated ERMCS spacing are wide-ranging for cell metabolism. We
391 detected changes in the mitochondrial generation of cellular energy, and in cellular lipids. Within
392 mitochondria, the OXPHOS electron transport chain undergoes changes in the balance between the
393 individual complexes. Most of these are depleted, while complex II resulted as increased upon
394 interference with TMX2. Interestingly, complex II accepts electrons from the Krebs cycle upon the
395 conversion of succinate to fumarate mediated by SUCLG1/SUCLG2 (Bezawork-Geleta et al., 2017).
396 Given that we observed a significant decrease of SUCLG1 in parallel, our findings indicate a
397 dysregulation of the succinate metabolism with low levels of TMX2. Succinate is thought to act as an
398 oncometabolite, which is associated with altered gene expression, and promotes growth (Selak et al.,
399 2005). Its expected deficiency upon TMX2 interference, resulting in decreased SUCLG1 and increased
400 complex II could therefore have the opposite effect and decrease growth and cell survival. This could
401 explain the association of increased TMX2 with breast cancer progression (Hatzidaki et al., 2020).
402 Similar to this hypothesis, the decreased presence of ether phospholipids, as observed with low levels of
403 TMX2 (Figure 7G), is expected to decrease lifespan (Cedillo et al., 2023) and associated with nervous
404 system defects in patients, including microcephaly and epilepsy (Dorninger et al., 2017). Ether lipids are
405 synthesized in peroxisomes and the ER (Dean & Lodhi, 2018), suggesting TMX2 could impact either
406 location. Likewise, the changes observed with HexCer, a class of ceramide species modified with
407 galactose or glucose, are another cause of mitochondrial ROS production due to the impaired activity of
408 ceramide transfer protein at the ER (Rao et al., 2014).

409 From the characterization of the redox and metabolic phenotype, we would predict that rescuing
410 succinate and ether phospholipid levels could provide a therapeutic avenue for the treatment of
411 NEDMCMS. To explore such possibilities, we could use our *in vivo* model, where we detected a
412 reproduction of the clinical features of this disease, comprising defective brain function and increased
413 epileptic readouts. Importantly, these defects were only manifest if TMX2 was reduced within glial cells.
414 Due to the similarity of NEDMCMS with other developmental epileptic encephalopathies, our findings

may extend to those diseases as well. For example, the ERMCS regulatory protein PACS-2 is mutated in developmental and epileptic encephalopathy-66 (DEE66 – MIM#618067) (Olson et al., 2018). Recent evidence showed that DEE66 results from increased availability of Ca^{2+} in the cytosol, which then activates synaptic vesicle release in neurons (Thi My Nhung et al., 2023). It remains to be shown whether the two diseases share a common mechanistic basis. Alternatively, the increased mitochondrial activity upon TMX2 interference could compromise normal levels of astrocytic lactate production, which is necessary for neuronal survival (Demetrius et al., 2014). Within this cell type, TMX2 could be part of the antioxidant response. This response is dependent on Nrf2, which is less active in neurons (Kraft et al., 2004). Alternatively, nuclear factor of activated T cells 1 (NFAT1) is known to induce ER antioxidant proteins including TMX1, TMX2 and GPx8 (Mognol et al., 2019) and promotes glial activation (Furman & Norris, 2014). Further experiments will have to determine whether Nrf2 or NFAT-1 control TMX2. Such insight could then be used to explore therapeutic approaches with the aim to rescue TMX2 and/or PRDX function. Any such approach should then restore neuronal Ca^{2+} availability that controls cell death and synaptic activity, as well as the metabolic pathology in glial cells.

Limitations of the Study

While our manuscript delineates the function of TMX2 for the formation of ERMCS, it currently does not clearly describe the biochemical activity of TMX2 for PRDX1. We provide data that demonstrate a partial replication of TMX2 depletion in NEDMCMS patient cells, but which function is critical for the pathology is unclear. The identification of glial cells as critical in our fly model needs to be validated in NEDMCMS.

Author contributions

Conceptualization: JC & TS; Data curation: JC, MCY, AB, DMP, TM, JZ, HM, & SGF; Formal analysis: JC, MCY, DMP, TM, JZ, & SGF; Funding acquisition: PCM & TS; Investigation: JC, MCY, AB, DMP, TM, JZ, HM, RB, SGF, YF, AZB & JM; Methodology: JC, MCY, AB, DMP, TM, JZ, PCM & TS; Project administration: TS; Resources: KB, LL, MO, MJL, HL, WHT, GMSM, BM, PCM & TS; Software: JC, AB, & TM; Supervision: PCM & TS; Validation: PCM & TS; Visualization: JC & MCY; Roles/Writing - original draft: TS; Writing - review & editing: JC, MJL, BM, PCM & TS.

Acknowledgments

We thank Tjakko J. van Ham, Peter Hwang and Leslie Poole for many helpful suggestions. We thank the following colleagues for critical reagents: Tito Cali for the SPLICS constructs, and Jennifer Rieusset for FATE-1. We are indebted to Xuejun Sun, Priscilla Gao and the Cell Imaging Facility at the Cross Cancer Institute/University of Alberta for assistance with microscopy. Funding for this study has been provided by CIHR operating grant PS162449 and CRS grant 834492 to TS. PCM is supported by operational funds from NSERC (Discovery Grant RGPIN-2023-05422). DMP is supported by the CIHR Canada Graduate Scholarship (CGS-M).

Declaration of Interests

The authors declare no competing interests.

458

459 **Figure Legends**

460

461 **Figure 1. TMX2 is a ER-mitochondria contacts (ERMCS) protein that maintains contact site**
462 **spacing.**

463 (A) Schematic overview of TMX2 membrane topology, as predicted by AlphaFold. Both N- and C-
464 termini localize to the cytosol. Limits of transmembrane domains are indicated by numbers. Position of
465 ER-lumenal and cytosolic portion are labeled. Cysteines are represented as yellow or green (catalytic
466 C170) models. (B) Protein sequence alignment of the TMX2 thioredoxin domain portion containing the
467 "SXXC" motif (highlighted in orange box) among species using the CLC Genomics Workbench
468 (QIAGEN). (C) Proteinase K digestion of two TMX2 variants (see cartoon) with the Flag-tag inserted at
469 amino acid 49 (version 1) or at the N-terminus (version 2). U251 MG cells expressing the two variants
470 were incubated with different concentrations of proteinase K and then subjected to immunoblot analysis
471 with Flag, TMX2, and calnexin antibodies. (D) Confocal immunofluorescence analysis of endogenous
472 TMX2 in U251 MG cells. Overlap between TMX2 and TOM70 signal is indicated in yellow. Scale bar,
473 20 μm. (E) Percoll membrane fractionation of TMX2 of U251 MG cells. Protein components of
474 subcellular fractions were analyzed by immunoblotting. Equal amounts were loaded and analyzed for the
475 indicated MAM-regulatory proteins (H: homogenate; ER: endoplasmic reticulum; MAM: mitochondria-
476 associated membrane; Mc: crude mitochondria; Mp: purified mitochondria; C: cytosol). (F) Co-
477 localization with ERMCS SPLICS probes. HeLa cells were transfected with SPLICS-short (ERMCS
478 distance 8-10 nm) or SPLICS-long (ERMCS distance 40-50 nm) plasmids and immunostained with
479 TMX2 antibody. Mander's coefficient analysis measured the co-localization between TMX2 and
480 SPLICS signals (n = 27-34 of 2 technical replicates for each group, ***$p < 0.001$ by unpaired t-test).
481 Scale bar, 20 μm. (G) Electron microscopy of TMX2 U251 MG wildtype and KO cells. Mitochondria
482 were labeled in red, and ER was labeled in green. Average ER-mitochondria distance, and total ERMCS
483 length were determined from electron micrographs (n = 75-91 of 3 technical replicates for each group,
484 ***$p < 0.001$ by Mann-Whitney U test). ERMCS were classified and quantified by the mean distance.
485 Scale bar, 0.5 μm.

486

487

488

489 **Figure 2. TMX2 interacts with TOM70 and promotes ERMCS spacing in a thioredoxin-like**
490 **domain-dependent manner.**
491 (A) Mitochondrial outer membrane (MOM) interactome. MOM proteins were extracted from the
492 interactome, and a protein-protein association network was generated with the STRING database
493 (https://string-db.org). Line color indicates the evidence of a functional association. (B) Co-
494 immunoprecipitation analysis. HEK293 cells were transfected with Flag-TMX2 for 48 h. The proteins
495 co-immunoprecipitated with Flag-TMX2 were then analyzed for calnexin and TOM70. (C) Interaction
496 between endogenous TMX2 and TOM70. Endogenous TOM70 was immunoprecipitated from HEK293
497 and analyzed for TMX2. (D) Transmission electron microscopy (TEM) analysis of TOM70 knock-down.
498 wild-type and TMX2-KO U251 MG cells transfected with TOM70 RNAi (siTOM70) for 48 h.
499 Mitochondria were labeled in red, and ER was labeled in green. Average ER-mitochondria distance, and
500 total ERMCS length were quantified [n = 59-219 of 3 technical replicates for each group, *p < 0.05, **p
501 < 0.01, and ***p < 0.001 by Kruskal-Wallis test (Dunn's multiple comparisons test)]. The ERMCS were
502 classified and quantified by the mean distance. Scale bar, 0.5 μm. (E) Co-immunoprecipitation analysis
503 of wild-type and C170S TMX2. HEK293 cells were co-transfected with Flag-TMX2-WT, Flag-TMX2-
504 C170S, and TOM70-HA for 24 h. The proteins co-immunoprecipitated with Flag-TMX2 were probed
505 with an HA antibody. (F) Transmission electron microscopy (TEM) analysis of TMX over-expression.
506 wild-type and TMX2-KO U251 MG cells transfected with TMX2 constructs as indicated for 48 h.
507 Mitochondria were labeled in red, and ER was labeled in green. Average ER-mitochondria distance, and
508 total ERMCS length were quantified [n = 59-219 of 3 technical replicates for each group, *p < 0.05, **p
509 < 0.01, and ***p < 0.001 by Kruskal-Wallis test (Dunn's multiple comparisons test)]. The ERMCS were
510 classified and quantified by the mean distance. Scale bar, 0.5 μm.
511
512 **Figure 3. TMX2 prevents TOM70 sulfenylation through PRDX1.**
513 (A) Cartoon depicting labeling of sulfenylated proteins with DCP-Bio1. The DCP-Bio1 reactive
514 carbon covalently attaches to a protein at its sulfenylation site. (B) DCP-Bio1 measurement of TOM70
515 sulfenylation in the presence of TMX2 RNAi. The assay was performed in HEK293 cells after
516 transfecting with TMX2 RNAi for 48 h. The sulfenylated cysteine residues were biotinylated and
517 immunoprecipitated with streptavidin beads. The immunoprecipitated proteins were then analyzed by
518 Western blotting with the indicated antibodies [n = 3 biological replicates for each group, *p < 0.001 by
519 unpaired t-test]. (C) Mass spectrometric analysis of sulfenylation modification within
520 immunoprecipitated TOM70. HEK293 isolates from control and TMX2 RNAi cells were used to detect

521 redox modifications, C206 was identified (n = 3 biological replicates). (D) PRDX interactions within the
522 TMX2 proteome. Interacting PRDXs were detected via CO-IP-MS analysis and visualized as a bubble
523 plot. The size of each bubble represents the relative abundance normalized to the empty vector group.
524 (E) PRDX1 interaction with TMX2. HEK293 cells were co-transfected with Flag-TMX2 and HA-
525 PRDX1 for 24 h. The proteins co-immunoprecipitated with HA-PRDX1 were probed with a Flag
526 antibody. (F) DCP-Bio1 measurement of TOM70 sulfenylation in the presence of TMX2 and PRDX
527 RNAi. HEK293 cells were transfected with the indicated RNAi for 48 h. Then the DCP-Bio1 assay was
528 performed and the immunoprecipitated proteins were analyzed by Western blots. (G) TOM70
529 interactome in wild-type and TMX2 U251 MG KO cells. CO-IP-MS analysis was subjected to
530 background subtraction, and the interactomes were plotted in a Venn diagram. (H) PRDX1 interaction
531 with TOM70 dependent on TMX2. In wild-type and TMX2-KO cells, the proteins co-
532 immunoprecipitated with the endogenous TOM70 were analyzed by Western blotting with the indicated
533 antibodies. (I) PRDX1 interaction with TOM70 dependent on TMX2 C170. TMX2-KO cells were
534 transfected with Flag-TMX2 and C170S plasmids for 48 h. Then the co-immunoprecipitation was
535 performed as described above.
536
537 **Figure 4. TMX2 alters ERMCS and limits ER-mitochondria Ca^{2+} transfer.**
538 (A) MAM proteome of U251 MG TMX2 wild-type and KO cells. MAM fractions were isolated
539 from wild-type and TMX2-KO cells by Percoll gradient fractionation, followed by LC-MS analysis to
540 detect the MAM proteomics altered under TMX2 depletion. The samples were then loaded on a precast
541 gel (50 μg protein each), digested, and the tryptic peptides were identified by Proteome Discoverer 2.5.
542 Data was normalized to each sample's total reconstructed peak area and the abundance of identified
543 proteins was represented by a heatmap (n = 2 biological replicates). (B) ER-mitochondria Ca^{2+} transfer
544 measurements. Wild-type and TMX2-KO cells and U251 cells stably transfected with TMX2 and its
545 mutants were transfected with the mitochondria-targeted and Ca^{2+} sensitive fluorescent probe Mito-
546 RGECO for 24 h. The Ca^{2+} signal was induced with 50 μm histamine (IP_3R activator). Relative
547 fluorescence increases were recorded and quantified [n = 62-143 of 3-4 biological replicates for each
548 group, **$p < 0.01$, and ***$p < 0.001$ by Mann-Whitney U test or Kruskal-Wallis test (Dunn's multiple
549 comparisons test)]. (C) Mitochondria Ca^{2+} content. Wild-type and TMX2-KO cells were transfected with
550 Mito-RGECO for 24 h, followed by incubating with 10 μM FCCP to block mitochondrial Ca^{2+} import.
551 Live-cell images were recorded and quantified (n = 47-96 of 3-4 biological replicates for each group, *p
552 < 0.05 by Mann-Whitney U test). (D) Representative immunofluorescence images of the proximity

553 ligation assay (PLA) between IP_3R1 and TOM70. HeLa cells were transfected with TMX2 RNAi for 48
554 h and subjected to the assay. The protein interactions (within 40 nm), visualized as a single dot, were
555 counted [n = 19-25 of 2 technical replicates for each group, ***p < 0.001 by one-way ANOVA (Dunnett's
556 multiple comparisons test)]. Scale bar, 20 μm. (E) ER Ca^{2+} content. ER Ca^{2+} leak under TBHQ (SERCA
557 pumps inhibitor) treatment was performed in wild-type and TMX2-KO cells, and U251 cells stably
558 transfected with TMX2 and its mutants after transfecting with ER-RGECO for 24 h. The drop of the
559 fluorescent signal is proportional to the ER Ca^{2+} content. The fluorescence was recorded and quantified
560 [n = 47-122 of 3-4 biological replicates for each group, *p < 0.05, and ***p < 0.001 by Mann-Whitney
561 U test or Kruskal-Wallis test (Dunn's multiple comparisons test)].
562
563 **Figure 5. TMX2 regulates cellular lipidomics and mitochondrial respiration.**
564 (A) U251 MG TMX2 KO lipidomics. Altered lipid species in U251 MG TMX2-KO cells (versus
565 wild-type) were visualized on a volcano plot. For each lipid molecule species, the abundance change
566 between wild-type and TMX2-KO cells on the x-axis against the p-value on the y-axis was plotted. The
567 significance was determined as FC >1.40 or <0.71, p-value <0.05, and p-value adjusted for false-
568 discovery rate (q-value) <0.25. The analysis showed 347 significantly up-regulated lipids with FC >1.40
569 and 370 significantly down-regulated lipids with FC <0.71 (n = 4 biological replicates for each group,
570 analyzed by unpaired t-test with Welch correction). (B) Heatmap for the relative abundance of the top 5
571 significantly altered PC and PE species. (C) Individual lipid species changes for PC (top) and PE
572 (bottom). PC and PE subtypes were classified (n = 4 biological replicates for each group, analyzed by
573 one-sample t-test). (D, E) Analysis of oxygen consumption rates in wild-type and TMX2-KO cells and
574 U251 MG cells stably expressing TMX2 mutants [n = 3 biological replicates for each group, *p < 0.05,
575 **p < 0.01, and ***p < 0.001 by two-way ANOVA (Dunnett's multiple comparisons test)]. (F) Cytosolic
576 ROS production in wild-type and TMX2-KO cells. CellROX™ Orange values were plotted (n = 3-4
577 biological replicates for each group, ***p < 0.001 by unpaired t-test). (G) Cytosolic ROS production
578 dependent upon the ERMCS spacer FATE-1. U251 MG cells were transfected with indicated siRNA
579 constructs for 24 h and further transfected with FATE-1-GFP for 48 h, and CellROX™ Orange values
580 were plotted [n =3 biological replicates for each group, ***p < 0.001 by two-way ANOVA (Šídák's
581 multiple comparisons test)]. (H) Cytosolic ROS production upon ER and mitochondrial ROS inhibition.
582 TMX2-KO cells were treated with 10 μm EN460 (ERO1 inhibitor), 5 μm GKT (NOX4 inhibitor), 15
583 μm S1QEL1.1 (Complex I inhibitor), 15 μm S3QEL 2 (Complex III inhibitor), and 25 μm Ru265 (MCU
584 inhibitor) overnight before analysis [n = 2-3 biological replicates for each group, **p < 0.01, and ***p

585 < 0.001 by one-way ANOVA (Dunnett's multiple comparisons test)] CellROX™ Orange values were
586 plotted.
587
588 **Figure 6. TMX2 maintains the normal mitochondrial proteome and function.**
589 (A) Changes in the mitochondrial proteome in U251 MG TMX2 KO cells. Volcano plots of
590 mitochondrial proteomics difference between wild-type and TMX2-KO cells. MitoCarta3.0 was used to
591 filter mitochondrial proteins, and representative TOM70 substrates. The significance was determined as
592 FC >2 or <0.5, and p-value <0.05 (n = 3 biological replicates for each group, analyzed by unpaired t-test
593 with Welch correction). (B) Further classification of mitochondrial proteome changes. Plots from A from
594 wild-type and TMX2-KO cells were further classified into subgroups (MOM: Outer mitochondrial
595 membrane; IMS: mitochondrial intermembrane space; MIM, Inner mitochondrial membrane; and
596 mitochondrial matrix). (C) Further classification of OXPHOS protein changes. The electron transport
597 chain (ETC) components were extracted from the dataset and analyzed (WT: open circles; TMX2-KO:
598 filled circles). (D) Western blot analysis of OXPHOS protein changes. The cell lysates from wild-type
599 and TMX2 were collected and analyzed with Western blots as indicated (n= 3 biological replicates for
600 each group, *p < 0.05, and **p < 0.01 by multiple unpaired t-test). (E) Correlation of TOM70 protein
601 interactions in U251 MG wild-type and TMX2 KO cells with TOM70 importome. Within the
602 interactome, TOM70 interacting mitochondrial proteins were determined (MitoCarta 3.0) were
603 determined in wild-type and TMX2-KO cells by CO-IP-MS analysis. The interactome was correlated to
604 the TOM70 importome (see text) [Black: non-mitochondrial proteins; Orange: localized to mitochondria
605 independently of TOM70; Light blue: localized to mitochondria, dependent on TOM70 (log_2FC import
606 *TOM70* KD/wild-type < 0); Dark blue: localized to mitochondria, dependent on TOM70 (log_2FC import
607 *TOM70* KD/wild-type < -0.5)]. (F) Transcription of select OXPHOS proteins. Gene expression
608 alterations of OXPHOS proteins between U251 MG wild-type and TMX2 KO cells were tested by RT-
609 qPCR analysis (n= 3 biological replicates for each group, statistics were performed via multiple unpaired
610 t-test). (G) OXPHOS pathway analysis. Wild-type and TMX2-KO cells were permeabilized with
611 digitonin, and then the mitochondrial respiration assays were performed (see Figure S6F). The
612 contribution of each ETC pathway (N, NADH; NS, NADH-Succinate; S, Succinate) to O_2 flux and flux
613 control ratio was measured and plotted [n = 3-4 biological replicates for each group, *p < 0.05, **p <
614 0.01, and ***p < 0.001 by two-way ANOVA (Šídák's multiple comparisons test)].
615
616

617

618 **Figure 7. *TMX2* mutant patient fibroblasts and glial *TMX2* knock-down *D.malanogaster***
619 **animals exhibit partial TMX2 loss of function.**

620 (A) Lysate analysis from control and NEDMCMS patient fibroblasts. Cell lysates were collected and
621 analyzed by Western blots with the indicated antibodies. (B) Representative electron microscopy images
622 of NEDMCMS patient fibroblasts. Mitochondria were labeled in blue, and ER was labeled in yellow.
623 Mitochondria circumference, average ER-mitochondria distance, and total ERMCS length were
624 measured from electron micrographs [n = 27-71 of 3 technical replicates for each group, *$p < 0.05$, and
625 ***$p < 0.001$ by Kruskal-Wallis test (Dunn's multiple comparisons test)]. The ERMCS were classified
626 and quantified by the mean distance. Scale bar, 0.5 µm. (C) Oxygen consumption rates in NEDMCMS
627 patient fibroblasts. High-resolution respirometry was performed to measure mitochondrial respiration of
628 NEDMCMS patient fibroblasts [n = 3-4 biological replicates for each group, **$p < 0.01$, and ***$p <$
629 0.001 by two-way ANOVA (Šídák's multiple comparisons test)]. (D) Cytosolic ROS levels in
630 NEDMCMS patient fibroblasts. Patient fibroblasts were treated with 10 µm EN460 (ERO1 inhibitor), 5
631 µm GKT (NOX4 inhibitor), 15 µm S1QEL1.1 (Complex I inhibitor), 15 µm S3QEL 2 (Complex III
632 inhibitor), and 25 µm Ru265 (MCU inhibitor) overnight. Then the cytosolic ROS production was
633 measured by flow cytometry [n = 3-6 biological replicates for each group, *$p < 0.05$, and ***$p < 0.001$
634 by two-way ANOVA]. CellROX™ Orange values were plotted. (E, F) Pan-glial knock-down of
635 *CG11007* (repo-GAL4 > UAS-CG11007-RNAi) at 25°C causes age-dependent climbing deficits and
636 mechanically-induced seizures in male and female flies at 20 days post-eclosion. This phenotype is not
637 observed in control flies (repo-GAL4 > UAS-luciferase-RNAi) or young animals at 5 days post-eclosion
638 [n = indicated in figure for each group, ****$p < 0.0001$ by one-way ANOVA (Tukey post-hoc test)]. (G)
639 Life span analysis of flies with pan-glial knock-down of *CG11007*. Kaplan Meier graph of male and
640 female animals, as indicated. ****$p < 0.0001$ by one-way ANOVA (Tukey post-hoc test).

641

642

643 **Supplemental Figure Legends**

644

645 **Figure S1. Supplementary information on basic TMX2 properties.**

646 (A) Glycosylation of endogenous TMX2. U251 MG cell lysates were treated with Endo H and
647 PNGase F for 60 min at 37°C. Samples were then analyzed with Ero1α and TMX2 antibodies. (B)
648 Glycosylation scanning analysis. HeLa cells were transfected with the indicated artificial glycosylation
649 mutants. Then, the glycosidase digestion assay was performed and the samples were analyzed with the
650 Ero1α and Flag antibodies. (C) 3D reconstruction of transfected Flag-tagged TMX2. HeLa cells were
651 transfected with Flag-TMX2-wild-type for 24 h. Then immunofluorescence microscopy was performed,
652 and TMX2 localization was observed after three-dimensional reconstruction (white arrow). Scale bar, 20
653 μm. (D) Percoll membrane fractionation of TMX2 in HeLa cells. Protein components of subcellular
654 fractions prepared were analyzed by immunoblotting. Equal amounts were loaded and analyzed for the
655 indicated ERMCS-regulatory proteins (H: homogenate; ER: endoplasmic reticulum; MAM:
656 mitochondria-associated membrane; Mc: crude mitochondria; Mp: purified mitochondria; C: cytosol).
657 (E) Redox dependence of TMX2 localization. After transfecting with Flag-TMX2-WT, HeLa cells were
658 treated with 200 μM H_2O_2 for 20 min or 5 mM NAC for 1h. Mander's coefficient analysis was utilized
659 to measure the co-localization between TMX2 and MitoTracker™ Red or Erp57 [n = 23-36 of 2 technical
660 replicates for each group, statistical analysis was performed with two-way ANOVA (Sidak's multiple
661 comparisons test)]. Scale bar, 20 μm. (F, G) TMX2 expression levels after knockout and knock-down.
662 TMX2-KO cells were generated with the CRISPR/Cas9 method using U251 MG cells. For TMX2 knock-
663 down, U251 MG cells were transfected with RNAi (siTMX2) using Oligofectamine. Experiments were
664 performed 48 h after transfection. The lysates were probed with a TMX2 antibody, and γ-tubulin served
665 as a loading control. (H) ERMCS analysis in U251 MG TMX2 control and knock-down cells.
666 Transmission electronic microscopy was performed with TMX2-KD cells. Mitochondria were labeled in
667 red, and ER was labeled in green. Mitochondria circumference, average ER-mitochondria distance, and
668 total ERMCS length were measured and analyzed [n = 69-166 of 3 technical replicates for each group,
669 *$p < 0.05$, **$p < 0.01$, and ***$p < 0.001$ by Kruskal-Wallis test (Dunn's multiple comparisons test)]. The
670 ERMCS were classified and quantified by the mean distance. Scale bar, 0.5 μm.

671

672

673

674 **Figure S2. Supplementary information on TMX2 interactome.**

675 (A) Pathway analysis of the TMX2 interactome. Interacting proteins were grouped using the
676 application Proteomap (http://bionic-vis.biologie.uni-greifswald.de/). Functionally related proteins are
677 grouped in similarly colored polygons, and the area size reflects protein abundance. (B) TOM70
678 expression levels upon knock-down. U251 MG wild-type and TMX2-KO cells were transfected with
679 TOM70 RNAi for 48 h, and then the cell lysates were subjected to the Western blot analysis using the
680 indicated antibodies. (C) Analysis of additional ER and mitochondrial interactors of wild-type and
681 mutant TMX2. Indicated TMX2 constructs (WT, C170S, and S167S mutants) were transfected and
682 immunoprecipitated. The relative abundance of interacting partners with TMX2-wild-type and its
683 mutants from the MS analysis was plotted as a bubble plot. Protein abundance was quantified with peak
684 areas, which were normalized to TMX2-WT. (D) Expression levels of transfected wild-type and mutant
685 TMX2 in HEK293 cells. The cell lysates extracted from the stable cell lines were subjected to the
686 Western blot analysis using the indicated antibodies.

687

688 **Figure S3. Supplementary data on TMX2-TOM70 interaction and effects on redox regulation.**

689 (A) Expression of TOM70 deletion mutants. HeLa cells were transfected with HA-tagged TOM70
690 truncations within the cytosolic domain (top), and the immunofluorescence microscopy was conducted
691 24 h after transfection. Scale bar, 20 μm. (B) Interaction of TMX2 with TOM70 deletion mutants. The
692 co-immunoprecipitation assay was performed using HEK293 cells co-transfected with Flag-TMX2-wild-
693 type and HA-tag TOM70 truncations for 24 h. Proteins associated with Flag-TMX2 were probed with a
694 HA antibody. (C) Assay to measure TMX2 oxidative activity. Cytosolic roGFP2-ScGrx1 oxidation was
695 measured in YPH499 Δ*glr1*Δ*grx1*Δ*grx2* cells (containing TMX2 plasmids) following the addition of
696 exogenous GSSG or exogenous H_2O_2 at the indicated concentrations. (D) Origin of ROS mediating
697 TOM70 sulfenylation in TMX2 knock-down cells. HEK293 cells were transfected with TMX2 RNAi for
698 48 h and treated with 15 μm S1QEL1.1 (Complex I inhibitor), 15 μm S3QEL 2 (Complex III inhibitor),
699 and 5 μm GKT (NOX4 inhibitor) for 20 h. Then the DCP-Bio1 assay was performed as described.

700

701 **Figure S4. Supplementary data on ERMCS proteome and Ca^{2+} flux.**

702 (A) Pathway analysis of up- and down-regulated MAM proteome in U251 MG TMX2 knockout
703 cells. Based on the MAM proteome data, pathway enrichment analysis was performed using the
704 Metascape database. A bar chart showed the representative term clusters altered in the absence of TMX2,
705 and the color represented the significance of the pathway enrichment. (B-E) Ca^{2+} responses from control

706 and TMX2 knock-down cells as indicated. (B) U251 MG cells were transfected with indicated siRNA
707 for 48 h and the plasmid encoding Mito-RGECO for 24 h. The Ca^{2+} signal was induced with 50 μm
708 histamine. Relative fluorescence increases were recorded and quantified [n = 31-55 of 3 biological
709 replicates for each group, statistics were performed via the Kruskal-Wallis test (Dunn's multiple
710 comparisons test)]. (C) U251 MG cells were transfected with indicated siRNA for 48 h and the plasmid
711 encoding Mito-RGECO for 24 h. Then the cells were incubated with 10 μM FCCP to block mitochondrial
712 Ca^{2+} import. Live-cell images were recorded and quantified [n = 33-75 of 2 biological replicates for each
713 group, statistics were performed via the Kruskal-Wallis test (Dunn's multiple comparisons test)]. (D)
714 U251 MG cells were transfected with indicated siRNA for 48 h and the plasmid encoding ER-RGECO
715 for 24 h. Then ER Ca^{2+} release under IP_3Rs activation (50 μm histamine) was performed. The
716 fluorescence drop was recorded and quantified [n = 50-62 of 2 biological replicates for each group, and
717 statistical analysis was conducted by the Kruskal-Wallis test (Dunn's multiple comparisons test)]. (E)
718 U251 MG cells were transfected with indicated siRNA for 48 h and ER-RGECO for 24 h. Then cells
719 were treated with 60 μM TBHQ, and the drop of the fluorescence signals was quantified (n = 21-31 of 2
720 biological replicates for each group, *p < 0.05 by Kruskal-Wallis test).
721
722 **Figure S5. Supplementary data on cellular lipidomics and mitochondrial respiration.**
723 (A) Lipidome analysis from U251 MG wild-type and TMX2 knockout cells. The class distribution
724 of the significantly altered lipid species (FC >1.40 or <0.71, p-value <0.05, and q-value <0.25) was
725 shown by the bar graph. (B) Oxygen consumption rate in U251 MG wild-type and TMX2 knock-down
726 cells. U251 MG cells were transfected with siRNA constructs for 48 h, and then mitochondria respiration
727 measurements were performed [n = 3 biological replicates for each group, ***p < 0.001 by two-way
728 ANOVA (Dunnett's multiple comparisons test)]. (C) Ca^{2+} and TOM70 dependence of altered respiration
729 in U-252 MG TMX2-KO cells. As indicated, cells were transfected with TOM70 RNAi for 48 h and
730 treated with 25 μM of Ru265 (MCU inhibitor) overnight. Then, high-resolution respirometry was
731 performed [n = 2-3 biological replicates for each group, *p < 0.05, **p < 0.01, and ***p < 0.001 by two-
732 way ANOVA (Dunnett's multiple comparisons test)]. (D-F) CellROX measurements as indicated. (D, E)
733 U251 MG cells transfected with siRNA constructs for 48 h and U251 MG cells stably expressing TMX
734 mutants were subjected to the measurements of cytosolic ROS production [n = 3 biological replicates for
735 each group, *p < 0.05, and ***p < 0.001 by one-way ANOVA (Dunnett's multiple comparisons test)].
736 (F) Wild-type and TMX2-KO cells were transfected with TOM70 RNAi for 48 h. Then, the cytosolic

737 ROS production was monitored via flow cytometry (n = 2 biological replicates for each group, *p < 0.05,
738 and ***p < 0.001 by two-way ANOVA (Dunnett's multiple comparisons test)].
739
740 **Figure S6. Supplementary information about mitochondrial proteome and function.**
741 (A) Correlation of protein abundance in the MS analysis of mitochondrial proteomes from wild-type
742 and TMX2-KO cells. The ratio of mitochondrial protein abundance between wild-type and TMX2-KO
743 cells was plotted in function of the protein abundance in wild-type cells. The ETC components were
744 labeled in red dots. The lines indicate that the abundance of the protein between wild-type and TMX2-
745 KO cells is the same. (B) Spacing reversal with FATE-1 does not revert U251 MG TMX2 knockcout
746 proteome. U251 MG wild-type and TMX2-KO cells were transfected with FATE-1 for 48 h. Then, the
747 cell lysates were collected and analyzed by Western blots with the indicated antibodies. (C)
748 Mitochondrial membrane potential analysis. Wild-type and TMX2-KO cells, and U251 MG cells
749 transfected with siRNA constructs for 48 h were used to measure mitochondrial membrane potential [n
750 = 3-4 biological replicates for each group, **p < 0.01, and ***p < 0.001 by unpaired t-test or one-way
751 ANOVA (Dunnett's multiple comparisons test)]. (D) Additional lysate analysis from U251 MG wild-
752 type and TMX2-KO cells. Cell lysates as indicated were collected and analyzed with Western blots with
753 the indicated antibodies. (E) ATP content analysis. U251 MG wild-type and TMX2-KO cells, and U251
754 MG cells transfected with siRNA constructs for 48 h were used for the ATP measurements [n= 2-3
755 biological replicates for each group, *p < 0.05, and ***p < 0.001 by unpaired t-test or two-way ANOVA
756 (Šídák's multiple comparisons test)]. (F) Mitochondrial pathway analysis. Representative trace of the O_2
757 flux in the digitonin-permeabilized wild-type and TMX2-KO cells. N-pathway (NADH-linked substrates
758 entering the ETC via complex I) was monitored after adding pyruvate+malate+glutamase (P+M+G) and
759 ADP. NS-pathway (electron flux convergence at Complexes I+II) was measured by the addition of
760 succinate (S). S-pathway (succinate entering the RTC through Complex II) was tested after inhibiting
761 Complex I with rotenone (Rot). Complex IV activity was measured in the presence of ascorbate (Asc)
762 and tetramethylphenylenediamine (TMPD), transferring electrons to complex IV. The chemical
763 background was subtracted after adding 100 mM sodium azide (Azd). Arrows indicate the time point of
764 adding the substrates or inhibitors. (G) Quantification of mitochondrial pathway analysis. U251 MG cells
765 were transfected with indicated siRNA for 48 h, and subjected to the mitochondrial respiration assay as
766 described [n = 3-4 biological replicates for each group, *p < 0.05, and **p < 0.01 by two-way ANOVA
767 (Dunnett's multiple comparisons test)].
768

769 **Figure S7. Supplementary data on *TMX2* mutant patient fibroblasts.**

770 (A) Summary of genetic variants and clinical characteristics in TMX2-linked patient fibroblasts.
771 Adapted from (Vandervore et al., 2019). (B) Lysate analysis from patient cells. The cell lysates from
772 patient fibroblasts were analyzed and probed with the indicated antibodies. (C) Mitochondrial membrane
773 potential analysis. TMRM signals of patient fibroblasts was measured via flow cytometry [n = 3
774 biological replicates for each group, *p < 0.05 by one-way ANOVA (Dunnett's multiple comparisons
775 test)]. (D) ATP content analysis. The ATP measurements were performed with patient fibroblasts [n = 3
776 biological replicates for each group, statistical analyses were performed by one-way ANOVA (Dunnett's
777 multiple comparisons test)]. (E-H) Assays from neuronal *CG11007* knockdown. (E, F) Pan-neuronal
778 knock-down of *CG11007* (nSyb-Gal4 > UAS-CG11007-RNAi) at 25°C does not cause any climbing
779 deficits or mechanically induced seizures in male and female flies at 20 days post-eclosion (n = 3
780 biological replicates for each group, statistical analyses were performed via unpaired t-test). (G, H)
781 Neuronal knock-down of CG11007 (nSyb-Gal4 > UAS-CG11007-RNAi) at 29°C leads to hyperkinetic
782 climbing in males but fails to cause climbing deficits or mechanically-induced seizures in aged male and
783 female flies at 20 days post-eclosion (n = 3 biological replicates for each group, **p < 0.01 by unpaired
784 t-test). (I) Mendelian ratios of *CG11007* glial knockdowns. Increasing the incubation temperature to 29°C
785 leads to significantly fewer repo-GAL4 > UAS- CG11007-RNAi that elcose from pupae than expected
786 [n = 3 biological replicates for each group, *p < 0.05 by one-way ANOVA (Tukey post-hoc test)]. (J, K)
787 High temperature analysis of glial *CG11007* knockdown. Pan-glial knock-down of *CG11007* (repo-
788 GAL4 > UAS- CG11007-RNAi) at 29°C causes climbing deficits, mechanically induced seizures in
789 young male and female flies at 5 days post-eclosion (n = 3 biological replicates for each group, ***p <
790 0.0001 by unpaired t-test).
791

792 **METHODS**

793

794

795 **EXPERIMENTAL MODEL AND STUDY PARTICIPANT DETAILS**

796

797 U251 MG cells (ATCC, US), HeLa cells (ECACC, UK), and HEK293 cells (ECACC, UK) were
798 cultured in DMEM (Gibco) with 10% fetal bovine serum (FBS; F1051, Sigma-Aldrich) at 37°C under
799 5% CO_2. Patient-derived skin fibroblasts were provided by Dr. Grazia M.S. Mancini's lab (Erasmus
800 University Medical Center, Netherlands) and Dr. Wen-Hann Tan's lab (Harvard Medical School, US),
801 which were grown under the conditions previously described (Vandervore et al., 2019).

802

803 All flies were raised on standard molasses-based food at 22 ºC unless otherwise indicated. The *nSyb-*
804 *Gal4* and *repo-Gal4* stocks were obtained from the Bloomington Drosophila Stock Center (BDSC) using
805 the following genotypes: y^1 w^*; *P[nSyb-GAL4.S]3* (BDSC_51635) and w^{1118}; *P[GAL4]repo/TM3,Sb1*
806 (BDSC_7415). The *UAS-luciferase RNAi* was described previously (Marcogliese et al., 2018). The *UAS-*
807 *CG11007 RNAi* (w^{1118}; *P[GD2093]v40833*) was obtained from the Vienna Drosophila Resource Center.

808

809 **METHOD DETAILS**

810

811 **DNA constructs and small interfering RNA (siRNA)**

812 The expression plasmids for C-terminally HA-tagged human TOM70, human Flag-TMX2 (N-
813 terminus, pcDNA3.1, wild-type and all mutants); human Flag-TMX2 (at 49 aa, pcDNA5, WT), and
814 human Flag-TMX2 (pIRES2-EGFP) were constructed by Genscript (Piscataway, NJ). Dog Flag-
815 Calnexin was previously described (Lynes et al., 2012). Plasmid-based transfection was performed with
816 Lipofectamine 3000 (Invitrogen) for U251 cells, and Metafectene Pro (Biontex) for HeLa and HEK293
817 cells, following the manufacturer's protocols. Cells were processed for experiments 24-48 h after
818 transfection.

819 For gene silencing, cells were transfected with the Stealth™ RNAi (12935300, Med GC) as a
820 negative control and siRNA (Invitrogen) to silence TMX2 or TOM70 expressions (siTMX2-1,
821 TMX2HSS121596, 5′-CCUAUCUAUGCUGACCUCUCCCUUA-3′; siTMX2-2, TMX2HSS181843,
822 5′-GGGAAGGUGGAUGUUGGACGCUAUA-3′; siTOM70-1, TOM70HSS114910, 5′-
823 GAAAUAGAUGCUGAAGGCAAAUACA-3′; siTOM70-2, TOM70HSS114911, 5′-

824 UGCUGUUGCAUGUACAUGCUGCCUC-3′; siTOM70-3, TOM70HSS114912, 5′-
825 AUAUGUUGUAGCAUUAUCUGGUUCC-3′;). Following the manufacturer's recommendations, RNA
826 interference was performed using Oligofectamine (Invitrogen). Cells were collected for experiments 48-
827 72 h after transfection.
828
829 **TMX2 CRISPR/Cas9 knockout**
830 U251 TMX2 KO cells were generated with the TMX2 Human Gene Knockout Kit (OriGene,
831 KN400032). The pCas-Guide vector (OriGene, GE100003) with a scrambled sequence was used as a
832 control. Briefly, U251 MG cells were co-transfected with a pCas-Guide vector (target sequence:
833 CCAACCTTACTACTACCTTCTGT) and a linear donor vector (containing EF1a-GFP-P1A-Puro)
834 using Lipofectamine 3000. Cells were grown for two weeks before the selection of puromycin (P8833,
835 Sigma-Aldrich). Then, the cells were transferred to 15-cm dishes, and individual cell colonies were
836 collected after culturing with 0.25 μg/mL puromycin for three weeks. The insertion of the donor vector
837 was verified by the presence of a GFP signal via flow cytometry, and TMX2 knockout was confirmed
838 by Western blot.
839
840 **Stable cell lines generation**
841 U251 cells were transfected with pIRES2-EGFP plasmids (empty vector, TMX2-WT, TMX2-
842 C170S, and TMX2-S167C) using Lipofectamine 3000. 24 h after transfection, cells were cultured with
843 1 mg/ml of Geneticin (10131027, Thermo Fisher Scientific). After 2 weeks, individual colonies were
844 selected and verified with Western blot and flow cytometry.
845
846 **Cell lysates and immunoblotting**
847 After washing 2 times with ice-cold 1× PBS (14080-055, Gibco), cells were trypsinized or scrapped
848 with a rubber policeman. Cells were then resuspended in m-RIPA lysis buffer [50 mM Tris-HCl (pH
849 7.4), 150 mM NaCl, 5 mM $MgCl_2$, 1% NP-40, 0.25% Sodium deoxycholate] containing 1× cOmplete
850 EDTA free protease inhibitor (11873580001, Roche) and 1× PhosSTOP phosphatase inhibitor
851 (4906845001, Roche), incubating on ice for 10 min. The lysates were then vortexed for 5 s and
852 centrifuged at 12,000 g for 15 min at 4°C to get post-nuclear supernatant. The protein concentration of
853 lysates was tested by the Pierce BCA Protein Assay Kit (23225, Thermo Fisher Scientific). For the
854 reducing gel, cell lysates were mixed with the sample loading buffer [60 mM Tris-HCl (pH 6.8), 2%
855 SDS, 10% glycerol, 5% β-mercaptoethanol, and 0.004% bromophenol blue] and boiled at 75°C for 8

856 min. For the non-reducing gel, the lysates were supplemented with 20 mM *N*-ethylmaleimide (NEM;
857 E3876, Sigma-Aldrich) and mixed with loading buffer without β-mercaptoethanol. The equal amounts
858 of protein per sample were loaded onto sodium dodecyl sulfate-polyacrylamide gel electrophoresis (SDS-
859 PAGE) gels. The gels were electrophoresed in the running buffer [25 mM Tris-HCl (pH 7.3), 200 mM
860 glycine, 0.1% SDS] for 75 min at 150 V, followed by transfer to nitrocellulose membranes (Bio-Rad) for
861 2 h at 400 mA. Then the membranes were blocked with 2% skimmed milk in TBST [10 mM Tris-HCL
862 (pH 8.0), 150 mM NaCl, 0.05% Triton X-100 (1086431000, Sigma-Aldrich)] for at least 30 min and then
863 kept with the primary antibodies overnight at 4°C. After washing 3 times with TBST, the membranes
864 were probed with secondary antibodies for 1 h. Then the membranes were washed with TBST and
865 scanned using an LI-COR Imager (CLX-2901, Biosciences). Image Lab Software (Bio-Rad) intensity
866 was used for band intensity quantification and analysis.
867
868 **Protease K protection assay**
869 U251 MG cells were transfected with two versions of Flag-TMX2-wild-type plasmids. The Flag-
870 tag was inserted following the putative signal peptide (Version 1) or at the N-terminus (Version 2). Cells
871 were harvested with homogenization buffer [20 mM HEPES (pH 7.4), 250 mM sucrose, 1 mM EDTA,
872 1 mM EGTA] in the presence of 1× protease inhibitor, followed by homogenization with a ball-bearing
873 homogenizer (ball clearance 14 μm, Isobiotec). Next, the lysates were spun at 2,000 rpm for 30 min at
874 4°C, using a JA-12 rotor (Beckman) to remove nuclei and unbroken cells. The post-nuclear supernatants
875 were centrifuged at 60,000 rpm for 60 min at 4°C with a TLA 120.2 rotor (Beckman) to collect ER-
876 mitochondria-enriched fractions. Pellets were resuspended in homogenization buffer, divided equally
877 into tubes, and treated with proteinase K (P8107, NE BioLabs) at different concentrations for 10 min at
878 room temperature (R.T.). The reaction was quenched by incubating with 4 mM phenylmethylsulfonyl
879 fluoride (PMSF; 52332, Sigma-Aldrich) for 5 min on ice. Then the samples were boiled at 75°C for 10
880 min in the loading buffer. All samples were sonicated and processed for SDS-PAGE and
881 immunoblotting.
882
883 **Percoll gradient fractionation**
884 HeLa and U251 MG cells were seeded in 15 cm dishes, collected with 5 ml of homogenization buffer
885 containing 1× protease inhibitor, and spun at 1,500 rpm for 5 min in a JA-12 rotor. Then cells were
886 resuspended in 5 ml homogenization buffer and passed 15-25 times through the homogenizer (ball
887 clearance 14 μm). The homogenates were centrifuged thrice at 2,000 rpm to remove unbroken cells and

888 nuclei. The supernatant was saved as a fraction of homogenate. The remaining supernatants were
889 centrifuged at 8,500 rpm for 10 min to obtain crude mitochondria fractions. Next, the resulting
890 supernatants were spun at 60,000 rpm for 60 min at 4°C in a TLA 120.2 rotor to acquire the fractions of
891 microsome (pellet) and cytosol (supernatant, incubation with ice-cold 100% acetone overnight). The
892 previously isolated crude mitochondria fractions were layered on the 18% Percoll gradient (GE17-0891-
893 02, Sigma-Aldrich) in OptiSeal polypropylene tubes (361623, Beckman). Then the samples were spun
894 at 33,300 rpm for 30 min with a 90Ti rotor (Beckman) to get the MAM and pure mitochondria fractions.
895 To remove the Percoll, the MAM fractions were spun at 60,000 rpm for 1 h using the TLA 120.2 rotor.
896 The fractions of pure mitochondria were transferred to tubes supplemented with homogenization buffer
897 and centrifugated twice at 10,000 g for 10 min, and the pellets were saved. Equal amounts of samples
898 were analyzed by immunoblotting, as previously described (Wieckowski et al., 2009).
899
900 **Mitochondria isolation**
901 Mitochondria were isolated from wild-type and TMX2 KO cells using the Mitochondria Isolation
902 Kit for Cultured Cells (89874, Thermo Fisher Scientific) according to the manufacturer's protocol
903 (Option A). Briefly, cells were harvested with PBS and centrifuged at 850 g for 2 min to obtain cell
904 pellets. 800 µL of Reagent A was added to each pellet, vortexed for 5 s at medium speed, and incubated
905 on ice for 2 min. Then the homogenate was added 10 µL of Reagent B and vortexed every minute at
906 maximum speed. Next, 800 µL of Reagent C was added to each tube and inverted multiple times to mix.
907 After centrifuging at 700 g for 10 min, the mitochondria-enriched supernatants were transferred to new
908 tubes and spun again at 12,000 g for 15 min at 4°C. Lastly, the isolated mitochondria pellets were washed
909 with 500 µL Reagent C, resuspended in homogenization buffer, and maintained on ice before
910 downstream experiments.
911
912 **Glycosidase Digestion**
913 The experiments were performed with U251 MG cells to test endogenous TMX2 and HeLa cells to
914 test TMX2 putative glycosylation mutants. On the experiment day, cells were lysed with glycoprotein
915 denaturing buffer (B1704S, NE BioLabs). Each sample was sonicated, denatured at 100°C for 10 min,
916 cooled on ice, and centrifuged for 10 s. The lysates were then treated with 500 U of peptide-N-
917 glycosidase F (PNGase F; P0704L, NE BioLabs) in a reaction solution containing 50 mM sodium
918 phosphate (pH 7.5) and 1% NP-40 (B2704S, NE BioLabs) for 1 h at 37°C. For endoglycosidase H (Endo
919 H; P0702S, NE BioLabs) digestion experiments, the cell lysates were deglycosylated with 500 U of Endo

920 H in the reaction buffer containing GlycoBuffer 3 (B1720S, NE BioLabs) for 1 h at 37°C. Then equal
921 amounts of samples were analyzed by immunoblotting, as described previously (Qiu et al., 2023).
922
923 **Immunoprecipitation**
924 For cross-linking immunoprecipitation, cells were incubated with 2 mM dithiobis(succinimidyl
925 propionate) (DSP; 22585, Thermo Fisher Scientific) in 1× PBS++(containing $CaCl_2$ and $MgCl_2$, diluted
926 from 10× PBS++, 1014200-075, Gibco) for 30 min at R.T. Next, cells were washed twice with PBS++
927 and quenched with 10 mM of NH_4Cl (A9434, Sigma-Aldrich) in PBS++ for 10 min at R.T. The cells
928 were then washed with PBS++ and harvested in RIPA lysis buffer. For co-immunoprecipitation, cells
929 were washed with PBS++ and collected in CHAPS lysis buffer [10 mM Tris (pH 7.4), 150 mM NaCl, 1
930 mM EDTA, 1% CHAPS] containing 20 mM NEM. Then the lysates were rocked for 30 min at 4°C and
931 centrifuged at 12,000 g for 15 min to pellet nuclei and unbroken cells. Preclearing was performed by
932 incubation with Protein G Magnetic Beads (10004D, Invitrogen) for 1 h at 4°C. Then the indicated
933 antibodies were added to the supernatants and rocked overnight at 4°C. Protein G Magnetic Beads were
934 added and rocked for 1 h at 4°C. The beads were washed 4 times with RIPA or CHAPS buffer, boiled in
935 the sample loading buffer at 75°C for 10 min, and analyzed by immunoblotting (Bassot et al., 2023).
936
937 **DCP-Bio1 assay for identification of sulfenylated proteins**
938 DCP-Bio1, consisting of the sulfenic acid-reactive 3-(2,4-dioxocyclohexyl) propyl (DCP) linked to
939 biotin, was used to capture the sulfenic acid formation (NS1226, Sigma-Aldrich) (Klomsiri et al., 2010,
940 Nelson et al., 2010). Briefly, HEK293 cells were cultured in 10-cm dishes and transfected with the
941 indicated RNAi for 48 h. After washing twice with PBS++ (containing 10 mM NEM), cells were lysed
942 in the reaction buffer [50 mM Tris-HCl (pH 7.5), 100 mM Sodium Chloride, 0.1% SDS, 0.5% Sodium
943 Deoxycholate, 0.5% NP-40, 0.5% Triton X-100] supplemented with 1 mM DCP-Bio1, 100 μM
944 Diethylene triamine pentaacetic acid (DTPA), 10 mM NEM, 1 mM PMSF, 200 U/mL catalase, and 1×
945 protease inhibitor. Samples were kept on ice for 30 min, followed by centrifugation at 16,000 g for 10
946 min at 4°C. Then the post-nuclear supernatants were kept on ice for 90 min in the dark for labeling of
947 the sulfenic acids. Zeba™ Spin Desalting columns (89890, Thermo Fisher Scientific) were pre-washed
948 3 times with CHAPS lysis buffer, loaded with the reacted samples, and spun at 1,000 g for 4 min at 4°C
949 to remove unreacted DCP-Bio1. Then protease inhibitor was added back to the lysates, and protein
950 concentration was determined by the BCA assay as described. Lysates were incubated with streptavidin
951 beads (65305, Invitrogen) overnight at 4°C. The beads were washed three times with CHAPS lysis buffer

952 and boiled in the sample loading buffer supplemented with 50 mM dithiothreitol (DTT; A22066A,
953 Invitrogen) for 10 min at 75°C. The lysates were analyzed by SDS-PAGE and Western blot.
954
955 ***In vitro* roGFP2 measurements**
956 YPH499 Δ*glr1*Δ*grx1*Δ*grx2* cells were co-transformed with a p415TEF plasmid encoding the
957 *Saccharomyces cerevisiae* plasma membrane glutathione transporter Opt1/Hgt1 and a p416TEF plasmid
958 encoding a genetic fusion construct consisting of roGFP2 and HsGrx1, *Hs*TMX2 or mutants thereof with
959 a short interspacing polypeptide linker (SGGGG × 5). Cells were grown to late logarithmic phase, OD_{600}
960 ≈ 3.0, in Hartwell's complete medium with 2% glucose and lacking leucine and uracil to facilitate
961 plasmid retention. For fluorescence measurements, cells were harvested at 1000 g for 3 min at R.T. and
962 resuspended in 100 mM MES/Tris buffer (pH=6) to an OD_{600} = 7.5. Subsequently, 200 µl aliquots were
963 transferred to the well of a flat-bottomed 96-well microtitreplate. The plate was centrifuged at 30 g for 5
964 min at R.T. so that the cells formed a loose pellet at the bottom of each well. The measurement was
965 initiated by the addition of H_2O_2 or GSSG at the indicated concentration and roGFP2 oxidation was
966 followed for another 30 min in a BMG Labtech CLARIOstar^{Plus} fluorescence plate reader.
967
968 RoGFP2 contains two redox-active cysteine residues on opposing β-strands adjacent to the
969 chromophore (Zimmermann et al., 2021). The formation of a disulfide bond between these cysteine
970 residues results in a ratiometric change in the fluorescence excitation spectrum of the roGFP2. The
971 neutral chromophore, which is predominant in disulfide bond-containing roGFP2, shows an excitation
972 maximum at ~400 nm, while the anionic chromophore, which is predominant in reduced roGFP2, is
973 excited with a maximum of ~490 nm. Excitation at both 400 nm and 490 nm results in fluorescence
974 emission with a maximum of ~510 nm, therefore, allowing ratiometric measurements. For roGFP2
975 calibration, 20 mM N, N-dimethylformamide (Diamide; D3648, Sigma-Aldrich), or 100 mM DTT were
976 added to the corresponding wells to obtain fully oxidized or fully reduced control samples. Probe
977 calibration allows for the determination of the degree of roGFP2 oxidation (OxD) according to the
978 equation below:
979 $$\mathrm{OxD}_{\mathrm{roGFP2}} = \frac{(I400sample * I480\mathrm{red}) - (I400\mathrm{red} * I480\mathrm{sample})}{(I400\mathrm{sample} * I480\mathrm{red} - I400\mathrm{sample} * I480\mathrm{ox}) + (I400\mathrm{ox} * I480\mathrm{sample} - I400\mathrm{red} * I480\mathrm{sample})}$$
980
981 **Mitochondrial Ca^{2+} measurements**
982 Live-cell imaging was performed with an Olympus FV1000 laser-scanning confocal microscope
983 using a 20× objective (XLUMPLANFL, NA 1.0, Olympus) (Gutierrez et al., 2020). The microscope was

984 equipped with a megapixel camera (PL-A686 6.6, PixeLink) and a perfusion system with a peristaltic
985 pump (Watson-Marlow Alitea-AB, Sin-Can). The flow speed was set at 6 ml per minute. Images were
986 obtained with the Olympus FluoView software and then analyzed with Fiji (NIH, USA) using the Time
987 Series Analyzer plugin (version 3.0).
988
989 The low-affinity Mito R-GECO fluorescent probe was used to measure mitochondrial Ca^{2+}. To
990 measure ER-mitochondria Ca^{2+} transfer, cells were cultured on the poly-L-lysine (P4707, Sigma-Aldrich)
991 coated 12-mm coverslips (Fisher Scientific) and transfected with the fluorescent plasmid. 24 h after
992 transfection, coverslips were transferred to the microscope chamber, perfusing with Hanks' balanced salt
993 solution (HBSS) with Ca^{2+} and Mg^{2+} (HBSS/Ca^{2+}/Mg^{2+}; 14025092, Thermo Fisher Scientific). After
994 establishing a baseline for 30 s, the perfusion buffer was replaced by HBSS/Ca^{2+}/Mg^{2+} supplemented
995 with 50 mM histamine (H7250, Sigma-Aldrich) for 5 min. To measure mitochondrial Ca^{2+} content, the
996 buffer was supplemented with 10 μM FCCP (15218, Cayman) for 15 min after establishing a
997 fluorescence baseline. Images were captured every second under histamine treatment and every 3 sec
998 under FCCP treatment in the Alexa 546 channel (559 nm excitation/575-675 nm emission).
999
1000 **ER Ca^{2+} measurements**
1001 ER R-GECO fluorescent probe was used to quantify ER Ca^{2+} content. Cells were prepared as
1002 mentioned above. After the first 30 s, the buffer was replaced with HBSS/Ca^{2+} free/Mg^{2+} free (14175095,
1003 Thermo Fisher Scientific) containing 60 μM tert-butylhydroquinone (TBHQ; 112941, Sigma-Aldrich),
1004 410 μM $MgSO_4$ (230391, Sigma-Aldrich), 1.75 μM $MgCl_2$ (MX0045-1, EM Science), and 100 μM
1005 EGTA (4100, OmniPur EMD) for 15 min to inhibit the activity of SERCA pump. Live-cell images were
1006 captured every 3 sec. As described previously, to measure Ca^{2+} release from ER, cells were perfused with
1007 50 mM histamine for 5 min, and images were captured every second in the Alexa 546 channel (559 nm
1008 excitation/575-675 nm emission).
1009
1010 **High-resolution respirometry**
1011 Cells were seeded in 6-well at least 48 h before experiments. The Oxygraph-2k machines (Oroboros
1012 Instruments, Innsbruck, Austria) were washed with 70% ethanol, 90% ethanol, and Milli-Q water. Then
1013 the oxygen was calibrated at 37°C, and the chambers were filled with 2 mL ice-cold DMEM, according
1014 to the manufacturer's instructions. For respirometry measurements in intact cells, cells were trypsinized
1015 and neutralized in fresh DMEM, followed by centrifugation at 350 g for 5 min at R.T. The cells were

1016 then resuspended in 2.6 mL of DMEM, and cell number was calculated. 2 mL of the intact cells were
1017 loaded into each chamber, and cellular respiration was recorded by measuring the oxygen flux. Briefly,
1018 basal respiration was measured without any added substrates. 2 μg/mL oligomycin (141829, Abcam)
1019 was added to inhibit ATP synthase and estimate the leak respiration. Maximal respiration was stimulated
1020 by the stepwise addition of the uncoupler carbonyl cyanide 4-(trifluoromethoxy)phenylhydrazone
1021 (FCCP; C2920, Sigma-Aldrich). Lastly, 0.25 μM antimycin A (A8674, Sigma-Aldrich) was added to
1022 inhibit Complex III and measure non-mitochondrial respiration.

1023 For permeabilized cell respiration, cells were counted and diluted in 2.6 mL of MiR05 buffer [110
1024 mM D-sucrose, 60 mM potassium lactobionate, 20 mM taurine, 20 mM HEPES, 10 mM KH_2PO_4, 3 mM
1025 $MgCl_2 \cdot 6H_2O$, 0.5 mM EGTA and 1 g/L fatty acid-free BSA (10775835001, Sigma-Aldrich), at pH 7.1].
1026 The digitonin concentration used for permeabilization was optimized before experiments. The following
1027 pathways were measured: NADH pathway (N-pathway, NADH-linked substrates, such as pyruvate and
1028 malate entering the chain at complex I) was measured after the addition of 5 mM pyruvate (P2256,
1029 Sigma-Aldrich) + 2 mM malate (M0875, Sigma-Aldrich) + 10 mM glutamate (G1626, Sigma-Aldrich)
1030 and 2.5 mM ADP (A5285, Sigma-Aldrich). NADH-Succinate pathway (NS-pathway, convergent
1031 electron flow at the Q-junction through Complexes I+II) was measured by the addition of 10 mM
1032 succinate (S2378, Sigma-Aldrich) (Mast et al., 2022). The succinate pathway (S-pathway; succinate
1033 entering the chain through complex II) was tested by inhibiting complex I with 0.5 μM rotenone (R8875,
1034 Sigma-Aldrich). After adding 0.5 mM tetramethyl phenylenediamine (TMPD; T3134, Sigma-Aldrich)
1035 and 2 mM ascorbate (A4034, Sigma-Aldrich), Complex IV activity was measured. The reduced state of
1036 TMPD was maintained by ascorbate to feed electrons into complex IV. Then the chemical background
1037 was subtracted after adding 100 mM sodium azide (S2002, Sigma-Aldrich). Mitochondrial respiration
1038 was determined by O_2 flux per cell and Flux Control Ratio (normalized to the maximal respiration).
1039 Datlab7 software (Oroboros Instruments) was used for data acquirement and analysis.
1040

1041 **Immunofluorescence microscopy**

1042 For standard immunofluorescence, cells were cultured on the poly-L-lysine-coated coverslips (18
1043 mm, thickness #1.5) in 6-well plates, as previously described. On the experiment day (24 or 48 h after
1044 transfection), cells were rinsed 3 times with PBS++ and fixed with 2% paraformaldehyde (PFA; 15710,
1045 Electron Microscopy Sciences) in PBS++ for 15 min at R.T. Then the cells were rinsed 3 times with
1046 PBS++ to quickly remove most of the fixative and quenched with 50 mM NH_4Cl for 10 min. Next, cells
1047 were washed with PBS++, permeabilized with 0.1% Triton X-100 in PBS++ for 10 min, and rinsed with

1048 PBS++ before blocking with 2% BSA in PBS++ for 1 h. Cells were then incubated with primary
1049 antibodies [rabbit anti-TMX2 (1:100, 19838-1-AP, Proteintech); mouse anti-TOM70 (1:150,
1050 H00009868-B01P, Abnova); mouse anti-Erp57 (1:100, SMC-168B, StressMarq); mouse anti-Flag
1051 (1:200, 200-301-B13, Rockland); rabbit anti-Flag (1:400, 14793, Cell Signaling); mouse anti-HA (1:200,
1052 901513, BioLegend)] for 1-2 h at R.T. in a humidified, light-protected chamber. After washing 3 times
1053 with PBS++ with 5 min rocking, cells were incubated with secondary antibodies [goat anti-Rabbit IgG
1054 (H+L), Alexa Fluor™ 594, A-11012, Invitrogen; goat anti-Mouse IgG2a, Alexa Fluor™ 488, A-11029,
1055 Invitrogen, at 1:1000], for at least 30 min. Cells were washed 3 times with PBS++, and coverslips were
1056 then mounted cell side down on the slides with ProLong™ Gold Antifade Mountant (P36934,
1057 Invitrogen). For mitochondrial morphology, cells were treated with 100 nM MitoTracker™ Red
1058 CMXRos probe (M7512, Thermo Fisher Scientific) for 30 min in the incubator before fixation. Nuclei
1059 were stained with 4′,6-diamidino-2-phenylindole dihydrochloride (DAPI; D9542, Sigma-Aldrich) for 5
1060 min at 1:1000.
1061
1062 The split-GFP-based contact site sensor (SPLICS) was designed to emit fluorescence when the ER
1063 and mitochondria are in proximity (Cali & Brini, 2021, Cieri et al., 2017). For co-localization analyses,
1064 two versions of SPLICS were used: SPLICS-short measures the organelle distances between 8 and 10
1065 nm, and SPLICS-long measures their contacts between 40 and 50 nm. HeLa cells were transfected with
1066 SPLICS-long or SPLICS-short plasmids. The next day, cells were cultured on the coverslips (18 mm)
1067 and immunostained, as mentioned previously, including fixation in 2% PFA for 15 min and blocking in
1068 2% BSA in PBS++. Mander's coefficient was calculated on raw images after background subtraction
1069 using ImageJ software (NIH, USA).
1070
1071 *In situ* proximity ligation assay (PLA) was performed to detect, visualize, and quantify protein
1072 interactions (within 40 nm) as a single dot (Tubbs et al., 2014). 24 h after gene silencing or plasmid DNA
1073 transfection, HeLa cells were cultured on the coverslips (18-mm). The next day, cells were fixed and
1074 incubated with anti-IP_3R1 (1:200, 3809289, Millipore) and VDAC1 (1:200, 14734, Abcam) or HA
1075 primary antibodies in a humidified chamber at 4°C overnight. Then the cells were washed twice with
1076 TBST, followed by incubating with the secondary antibodies (anti-Mouse MINUS, DU092004, Sigma-
1077 Aldrich; anti-Rabbit PLUS, DUO92002, Sigma-Aldrich) for 1 h at 37°C. The proximity ligation and
1078 polymerase amplification steps followed the manufacturer's protocols (Duolink® In Situ Detection
1079 Reagents Red, DU092008, Sigma-Aldrich). Note that the 5× ligase and 5× polymerase were diluted and

1080 added immediately before addition to the samples. Then the cells were stained with DAPI and actin
1081 (1:1000, 176753, Abcam). Images were deconvolved, and the number of dots per nucleus was quantified
1082 with ImageJ software as described previously (Tubbs & Rieusset, 2016). Experiments were repeated
1083 twice, and at least 8 fields were taken in each condition.
1084
1085 Images were obtained with a Leica SP8 Falcon microscope (100× 1.4 NA oil immersion lens). The
1086 Leica TCS SP8 microscope was equipped with the Leica Application Suite X Software (version 3.5).
1087 Between 4 and 8 z-stack images were captured with 200-400 nm step size. 488 nm excitation was used
1088 for SPLICS fluorescence and Alexa 488-labeled antibodies. 594 nm excitation was used for
1089 MitoTracker™, PLA dots, and Alexa 594-labeled antibodies. A 405 nm laser was used for DAPI
1090 excitation. After background signal subtraction, maximum intensity projection was selected to acquire
1091 the summed intensities.
1092
1093 **Transmission electronic microscopy (TEM)**
1094 After gene silencing or plasmid DNA transfection, cells were seeded on the ACLAR® Film (10501,
1095 TED PELLA, INC) to 80% confluence. Cell monolayers were fixed with 2% PFA and 2.5%
1096 glutaraldehyde (GTA; G5882, Sigma-Aldrich) in 0.15 M cacodylate solution (C0250, Sigma-Aldrich)
1097 with 2 mM $CaCl_2$ for 20 min at 37°C and 40 min at R.T. Post fixation was done with 2% osmium tetroxide
1098 (OsO_4; 201030, Sigma-Aldrich) in 1.5% potassium ferrocyanide with 2 mM $CaCl_2$ (freshly prepared
1099 before use) for 1 h on ice. Then the samples were treated with filtered thiocarbohydrazide (TCH; 223220,
1100 Sigma-Aldrich) solution for 20 min at R.T., 2% OsO_4 for 30 min at R.T., and washed with ddH_2O before
1101 staining with 1% uranyl acetate overnight at 4°C on a rocker. The next day, the samples were stained
1102 with Lead Nitrate in the aspartic acid solution for 30 min at 60°C. Then the samples were dehydrated
1103 with increasing concentrations of ice-cold ethanol (20%, 50%, 70%, and 90% ethanol 5 min each, 100%
1104 ethanol 5 min twice) and infiltrated with acetone for 10 min × 2 at R.T. Samples were embedded with
1105 Durcupan™ ACM (44611, Sigma-Aldrich) and polymerized at 60°C oven for 48 h before sectioning. A
1106 Transmission Electron Microscope (TEM) from JEOL (JEM-2100) equipped with a Lab6 filament at
1107 200 kV acceleration voltage was used for TEM observation of the samples. The system is operated with
1108 a Gatan GIF Quantum energy filter using a 2k × 2k digital camera with DigitalMicrograph software
1109 (version 2.0). The images were taken with a resolution of 2048 × 2048 pixels. Images were quantitatively
1110 analyzed for ER and mitochondria contacts (within 50 nm) with imageJ, as described previously (Bassot

1111 et al., 2023, Theurey et al., 2016). Data was generated from at least 30 images per condition with around
1112 100 measurements each.
1113
1114 **Cellular ATP measurements**
1115 Cells were cultured in 12-well plates and reached 80% confluence on the experiment day. Cells were
1116 incubated with or without 3 μM oligomycin to estimate mitochondrial ATP production for 1.5 h. Cells
1117 were then trypsinized and resuspended in the CHAPS lysis buffer containing 1× protease inhibitor.
1118 Cellular ATP content was measured by the ATP Determination kit (A22066, Molecular Probes)
1119 following the manufacturer's instructions, which measured ATP by recombinant the firefly luciferase
1120 and its substrate D-luciferin. Then the luminescence (emission maximum 560 nm at pH 7.8) was
1121 monitored with a Synergy 4 plate reader (Bio Tek), and the ATP levels were normalized to protein
1122 concentrations (Gutierrez et al., 2020).
1123
1124 **Flow cytometry**
1125 Cytosolic ROS, mitochondrial ROS, and mitochondrial membrane potential were measured using a
1126 BD LSR Fortessa-SORP flow cytometer (BD Biosciences). Briefly, cells were incubated with 0.5 μM
1127 CellROX™ Orange (C10493A, Invitrogen) for 1 h or 1 μM MitoSOX™ (M36008, Invitrogen) for 40
1128 min at 37°C. Then the cells were collected and resuspended in 300 μL HBSS/Ca^{2+} free/Mg^{2+} free
1129 supplemented with 0.5% bovine serum albumin (BSA; A6003, Sigma-Aldrich). Single, live cells of
1130 interest were gated on the forward scatter (FSC) and side scatter (SSC) plots. The gates were determined
1131 by control groups, treating cells with either 400 μM tert-butyl hydroperoxide (TBHP; C10493A,
1132 Invitrogen) or 5 mM N-acetyl-L-cysteine (NAC; A9165, Sigma-Aldrich) for 1 h at 37°C. Then the
1133 fluorescence intensity of CellROX™ Orange (545 nm excitation/565 nm emission) and MitoSOX™ (510
1134 nm excitation/ 580 nm emission) were measured. Mitochondrial membrane potential was tested after
1135 incubating cells with 40 nM tetramethylrhodamine, methyl ester (TMRM, T668, Invitrogen) for 30 min
1136 at 37°C. The gates were adjusted by treating cells with 3 μM oligomycin or 10 μM FCCP for 1.5 h. Then
1137 the TMRM fluorescence intensity was measured (552 nm excitation/579 nm emission). Mean
1138 fluorescence intensity was determined, and data analysis was performed with the BD FACSDiva™
1139 software.
1140
1141 **The RNA extraction and RT-qPCR**
1142

1143 The total RNA was extracted using TRIzol (Life Technologies) following the manufacturer's
1144 protocol. Two micrograms of total RNA were subjected to reverse transcription using the Superscript II
1145 kit (Life Technologies) and the random primers (Life Technologies). The relative gene abundance in the
1146 cDNA sample was examined by the quantitative PCR (qPCR) experiment on Mastercycler Realplex^2
1147 (Eppendorf) using PerfeCTa SYBR green PCR mix (Quanta Bioscience). Oligonucleotides for the
1148 reaction were summarized in Table X. The change in the mRNA level of the genes among various
1149 mutants was evaluated by the comparative C_T method (Schmittgen & Livak, 2008). The C_T value for
1150 each gene target was normalized against the internal control (ACTB) to give the ΔC_T value. The $\Delta\Delta C_T$
1151 for each gene was calculated as a difference in ΔC_T values between the wild-type and the TMX2-KO
1152 cells. The difference in gene mRNA levels between wild-type and TMX2-KO cells was given as $2^{-\Delta\Delta CT}$,
1153 based on the assumption that the amplification efficiency of the PCR reaction is 100%.
1154
1155 **Liquid chromatography-mass spectrometry (LC-MS)**
1156 MAM and mitochondria proteomics altered in the absence of TMX2 were quantified by LC-MS.
1157 MAM and mitochondria samples were isolated as described above. The isolated mitochondria pellets
1158 were incubated with or without 40 µg/ml proteinase K for 30 min at R.T. The reaction was stopped by
1159 adding 4 mM PMSF for 5 min on ice. Samples were sonicated, and 50 µg of each was loaded and ran on
1160 the precast gels (4561034, Bio-Rad), stained with Coomassie blue P-250 (161-0436, Bio-Rad), and
1161 started the in-gel digestion process (Rashed et al., 2021). Briefly, gel fragments were destained twice in
1162 the ammonium bicarbonate/acetonitrile (50:50) solution. Then the samples were reduced with DTT and
1163 alkylated with iodoacetamide, followed by digestion with the sequencing grade modified trypsin (V5111,
1164 Promega) overnight at 37°C. Tryptic peptides were extracted from the gel with 97% water, 2%
1165 acetonitrile (047138-M1, Thermo Fisher Scientific), 1% formic acid (270480025, Thermo Fisher
1166 Scientific), and then a further extraction with the previous extraction buffer and acetonitrile (50:50). For
1167 the IP-MS, proteins were cross-linked with 2 mM DSP as described previously and immunoprecipitated
1168 using Anti-Flag® M2 Magnetic Beads (M8823, Sigma-Aldrich) or protein targeted primary antibodies
1169 and Protein G Magnetic Beads. Trypsin digestions were performed on a KingFisher™ Duo Prime
1170 Purification System (Thermo Fisher Scientific). Samples were reduced and alkylated (DTT,
1171 iodoacetamide) before digestion with the sequencing grade modified trypsin for 10 h at 37°C.
1172
1173 The tryptic peptides were resolved with the EASY-nLC 1000 (Thermo Fisher Scientific) connected
1174 to the Q-Exactive Orbitrap mass spectrometer (Thermo Fisher Scientific) with an EASY-Spray™

1175 capillary HPLC column (75 µm × 25 cm, 100Å, 2 µm; ES902A, Thermo Fisher Scientific). The mass
1176 spectrometer was operated in data-dependent acquisition (DDA) mode with a m/z range of 300-1700 and
1177 35,000 resolution. By using HCD dissociation, the 12 most intense multiply charged ions were
1178 sequentially fragmented, and their fragments spectra were recorded in the orbitrap at 17,500 resolution.
1179 For identification of the sulfenylated cysteines, peptides were resolved using an EASY-Spray capillary
1180 HPLC column (ES902A, 75 µm × 25 µm, 100Å, 2µm, Thermo Scientific) and a Vanquish Neo UHPLC
1181 (Thermo Fisher Scientific) coupled to an Orbitrap Exploris 480 mass spectrometer (Thermo Scientific).
1182 The mass spectrometer was operated in data-dependent acquisition mode with a resolution of 60,000,
1183 an m/z range of 350–1700, and a cycle time of 3 seconds. Selected ions were fragmented by HCD
1184 dissociation, and spectra of their fragments were recorded in the orbitrap at a resolution of 15,000. After
1185 fragmentation, all precursors selected for dissociation were dynamically excluded for 30 s.
1186
1187 Data was analyzed with Proteome Discoverer 2.5 (Thermo Fisher Scientific), and a human proteome
1188 database (UniProt) was screened with SEQUEST (Thermo Fisher Scientific). The normalization node
1189 was added to the processing workflow. A false discovery rate (FDR) between 0.01 and 0.05, a fragment
1190 mass tolerance of 0.01 Da, and a precursor mass tolerance of 10 ppm were involved in the search
1191 parameters. In addition, peptides were screened for modifications such as carbamidomethyl cysteine,
1192 sulfenylated cysteine, oxidized methionine, as well as deamidated glutamine and asparagine.
1193 Mitochondrial annotations were matched with the MitoCarta3.0 data set (Rath et al., 2021), and TOM70
1194 substrates were extracted and compared according to the previous publications (Morgenstern et al.,
1195 2021).
1196
1197 **Lipidome Profiling by UHPLC−MS**
1198 For lipidomic analysis, wild-type and TMX2 KO cells were harvested and washed 3 times with pre-
1199 cooled PBS (1.25×10^7 cells/sample). Next, the tubes with cell pellets were kept in liquid nitrogen for 2
1200 min to stop the metabolism and stored in a -80 °C freezer (protection from light for further use). Lipids
1201 extraction was performed strictly following a modified Folch liquid-liquid extraction protocol (Zardini
1202 Buzatto et al., 2020). Briefly, samples were mixed with NovaMT LipidRep internal standard solution (a
1203 mixture of 15 deuterated lipid standards), dichloromethane and methanol. After homogenization and
1204 cleaning with water, samples were equilibrated for 10 min at R.T. and spun at 16,000 g for 10 min at
1205 4°C. An organic layer was harvested and evaporated to dryness using a nitrogen blowdown evaporator.
1206 Dried samples were then resuspended in NovaMT MixB, vortexed for 1 min, and diluted with NovaMT

1207 MixA (Nova Medical Testing Inc., Edmonton, Canada). For quality control (QC), a pooled mixture
1208 randomly extracted from each sample was prepared.
1209
1210 LC-MS/MS was performed in positive and negative ionization to identify and quantify the extracted
1211 lipids. A Thermo Vanquish UHPLC linked to Bruker Impact II QTOF Mass Spectrometer was used,
1212 equipped with a Waters Acquity CSH C18 column, 1.7 µm (Thermo Fisher Scientific). MS/MS spectra
1213 were acquired for sample alignment, and identification was processed by NovaMT LipidScreener.
1214 MS/MS peaks were identified by a three-tier identification approach based on MS/MS spectral similarity,
1215 retention time, and accurate mass match (Tier 1: MS/MS match score ≥500, precursor m/z error ≤20.0
1216 ppm, 5.0 mDa; Tier 2: MS/MS match score <500; precursor m/z error ≤20.0 ppm, 5.0 mDa; Tier 3: Mass
1217 match with m/z error ≤20.0 ppm and 5.0 mDa) (Easton et al., 2023). All compounds identified in these
1218 tiers were utilized for normalization and data analysis. The identified lipids were class-matched to the
1219 most similar internal standards (15 deuterated lipid standards) and median-normalized. Unidentified
1220 features were saved for further investigation but not employed for statistics. Statistical analysis was
1221 performed with NovaMT LipidScreener. Non-informative features were filtered out during data
1222 processing.
1223
1224 **Drosophila mendelian ratios and lifespan**
1225 Progeny counts for control (*UAS-luciferase RNAi*) and experimental (*UAS-CG11007 RNAi*) flies and
1226 lifespan analysis was performed as previously described (Marcogliese et al., 2018). Briefly, for repo-
1227 Gal4 crosses, flies lacking the balancer: TM3, Sb1 had both the Gal4 and UAS-RNAi present making
1228 the expected genotype 50%. For at least three independent crosses the observed/expected number of flies
1229 was recorded. Because *nSyb-Gal4* is homozygous viable, 100% of F1 progeny are the appropriate
1230 genotype for *nSyb>luciferase RNAi* or *nSyb>CG11007 RNAi*. For lifespan, flies of the correct genotypes
1231 and separated by sex were aged at indicated temperatures. Flies were transferred to new vials every 3
1232 days. Flies were assessed for lethality every day.
1233
1234 **Drosophila behavior**
1235 Both climbing (negative geotaxis) and mechanical seizure induction (bang-sensitivity) were
1236 performed as previously described (Marcogliese et al., 2022). Briefly, 24 h before testing, flies are
1237 individually housed in vials with 1 mL of food. On the day of testing, flies are transferred to a clean
1238 empty vial and allowed to habituate for 1 min. After habituation, the vial is tapped on the bench to induce

negative geotaxis behavior and the fly the time to climb 7 cm is assessed. Flies that failed to cross the 7 cm line were given a score of 30. Following negative geotaxis, the bang-sensitivity assay was performed by vortexing flies for 15 s at maximum speed to determine if there are any paralysis or spastic behavior after vortexing. The researcher is blinded to genotype and drug. Total n derives from three independent crosses.

Data analysis

Statistical analyses were performed with GraphPad Prism® 9.0 software (US). Values are expressed as mean ± SD. The Shapiro-Wilk test and QQ plots were performed to check data normality. For normally distributed data, unpaired t-test, one-way, and two-way analysis of variance (ANOVA) were performed. For non-normally distributed data, the Mann-Whitney U test was used to compare differences between two groups, and the Kruskal-Wallis test was used for three or more independent groups. Statistical significance was determined as $p < 0.05$.

KEY RESOURCES TABLE

See separate document.

REFERENCES

Arner ES, Holmgren A (2000) Physiological functions of thioredoxin and thioredoxin reductase. Eur J Biochem 267: 6102-9

Backes S, Bykov YS, Flohr T, Raschle M, Zhou J, Lenhard S, Kramer L, Muhlhaus T, Bibi C, Jann C, Smith JD, Steinmetz LM, Rapaport D, Storchova Z, Schuldiner M, Boos F, Herrmann JM (2021) The chaperone-binding activity of the mitochondrial surface receptor Tom70 protects the cytosol against mitoprotein-induced stress. Cell Rep 35: 108936

Bassot A, Chen J, Takahashi-Yamashiro K, Yap MC, Gibhardt CS, Le GNT, Hario S, Nasu Y, Moore J, Gutierrez T, Mina L, Mast H, Moses A, Bhat R, Ballanyi K, Lemieux H, Sitia R, Zito E, Bogeski I, Campbell RE et al. (2023) The endoplasmic reticulum kinase PERK interacts with the oxidoreductase ERO1 to metabolically adapt mitochondria. Cell Rep 42: 111899

Beretta M, Santos CX, Molenaar C, Hafstad AD, Miller CC, Revazian A, Betteridge K, Schroder K, Streckfuss-Bomeke K, Doroshow JH, Fleck RA, Su TP, Belousov VV, Parsons M, Shah AM (2020) Nox4 regulates InsP3 receptor-dependent Ca(2+) release into mitochondria to promote cell survival. EMBO J 39: e103530

Bezawork-Geleta A, Rohlena J, Dong L, Pacak K, Neuzil J (2017) Mitochondrial Complex II: At the Crossroads. Trends Biochem Sci 42: 312-325

Booth DM, Enyedi B, Geiszt M, Varnai P, Hajnoczky G (2016) Redox Nanodomains Are Induced by and Control Calcium Signaling at the ER-Mitochondrial Interface. Mol Cell 63: 240-8

Booth DM, Varnai P, Joseph SK, Hajnoczky G (2021) Oxidative bursts of single mitochondria mediate retrograde signaling toward the ER. Mol Cell 81: 3866-3876 e2

Cali T, Brini M (2021) Quantification of organelle contact sites by split-GFP-based contact site sensors (SPLICS) in living cells. Nat Protoc 16: 5287-5308

Cardenas C, Miller RA, Smith I, Bui T, Molgo J, Muller M, Vais H, Cheung KH, Yang J, Parker I, Thompson CB, Birnbaum MJ, Hallows KR, Foskett JK (2010) Essential regulation of cell bioenergetics by constitutive InsP3 receptor Ca2+ transfer to mitochondria. Cell 142: 270-83

Cedillo L, Ahsan FM, Li S, Stuhr NL, Zhou Y, Zhang Y, Adedoja A, Murphy LM, Yerevanian A, Emans S, Dao K, Li Z, Peterson ND, Watrous J, Jain M, Das S, Pukkila-Worley R, Curran SP, Soukas AA (2023) Ether lipid biosynthesis promotes lifespan extension and enables diverse pro-longevity paradigms in Caenorhabditis elegans. Elife 12

Chen Z, Ho IL, Soeung M, Yen EY, Liu J, Yan L, Rose JL, Srinivasan S, Jiang S, Edward Chang Q, Feng N, Gay JP, Wang Q, Wang J, Lorenzi PL, Veillon LJ, Wei B, Weinstein JN, Deem AK, Gao S et al. (2023) Ether phospholipids are required for mitochondrial reactive oxygen species homeostasis. Nat Commun 14: 2194

Chen Z, Lei C, Wang C, Li N, Srivastava M, Tang M, Zhang H, Choi JM, Jung SY, Qin J, Chen J (2019) Global phosphoproteomic analysis reveals ARMC10 as an AMPK substrate that regulates mitochondrial dynamics. Nat Commun 10: 104

Cieri D, Vicario M, Giacomello M, Vallese F, Filadi R, Wagner T, Pozzan T, Pizzo P, Scorrano L, Brini M, Cali T (2017) SPLICS: a split green fluorescent protein-based contact site sensor for narrow and wide heterotypic organelle juxtaposition. Cell Death Differ

Cieri D, Vicario M, Giacomello M, Vallese F, Filadi R, Wagner T, Pozzan T, Pizzo P, Scorrano L, Brini M, Cali T (2018) SPLICS: a split green fluorescent protein-based contact site sensor for narrow and wide heterotypic organelle juxtaposition. Cell Death Differ 25: 1131-1145

Davie K, Janssens J, Koldere D, De Waegeneer M, Pech U, Kreft L, Aibar S, Makhzami S, Christiaens V, Bravo Gonzalez-Blas C, Poovathingal S, Hulselmans G, Spanier KI, Moerman T,

1304 Vanspauwen B, Geurs S, Voet T, Lammertyn J, Thienpont B, Liu S et al. (2018) A Single-Cell
1305 Transcriptome Atlas of the Aging Drosophila Brain. Cell 174: 982-998 e20
1306 Dean JM, Lodhi IJ (2018) Structural and functional roles of ether lipids. Protein Cell 9: 196-206
1307 Demetrius LA, Magistretti PJ, Pellerin L (2014) Alzheimer's disease: the amyloid hypothesis and
1308 the Inverse Warburg effect. Front Physiol 5: 522
1309 Dorninger F, Forss-Petter S, Berger J (2017) From peroxisomal disorders to common
1310 neurodegenerative diseases - the role of ether phospholipids in the nervous system. FEBS Lett 591:
1311 2761-2788
1312 Dupuy E, Van der Verren SE, Lin J, Wilson MA, Dachsbeck AV, Viela F, Latour E, Gennaris A,
1313 Vertommen D, Dufrene YF, Iorga BI, Goemans CV, Remaut H, Collet JF (2023) A molecular device
1314 for the redox quality control of GroEL/ES substrates. Cell 186: 1039-1049 e17
1315 Easton ZE, Regnault TRH, Mudri M, Zhao S, Smith SA, Zardini Buzatto A, Li J, Duruisseau-
1316 Kuntz R, Davidson J, Li L, Butter A (2023) The metabolic and lipidomic profiling of the effects of
1317 tracheal occlusion in a rabbit model of congenital diaphragmatic hernia. J Pediatr Surg 58: 971-980
1318 Filadi R, Leal NS, Schreiner B, Rossi A, Dentoni G, Pinho CM, Wiehager B, Cieri D, Cali T,
1319 Pizzo P, Ankarcrona M (2018) TOM70 Sustains Cell Bioenergetics by Promoting IP3R3-Mediated ER
1320 to Mitochondria Ca(2+) Transfer. Curr Biol 28: 369-382 e6
1321 Furman JL, Norris CM (2014) Calcineurin and glial signaling: neuroinflammation and beyond. J
1322 Neuroinflammation 11: 158
1323 Ganji R, Paulo JA, Xi Y, Kline I, Zhu J, Clemen CS, Weihl CC, Purdy JG, Gygi SP, Raman M
1324 (2023) The p97-UBXD8 complex regulates ER-Mitochondria contact sites by altering membrane lipid
1325 saturation and composition. Nat Commun 14: 638
1326 Ghosh SG, Wang L, Breuss MW, Green JD, Stanley V, Yang X, Ross D, Traynor BJ, Alhashem
1327 AM, Azam M, Selim L, Bastaki L, Elbastawisy HI, Temtamy S, Zaki M, Gleeson JG (2020) Recurrent
1328 homozygous damaging mutation in TMX2, encoding a protein disulfide isomerase, in four families
1329 with microlissencephaly. J Med Genet 57: 274-282
1330 Giacomello M, Pellegrini L (2016) The coming of age of the mitochondria-ER contact: a matter of
1331 thickness. Cell Death Differ 23: 1417-27
1332 Gilady SY, Bui M, Lynes EM, Benson MD, Watts R, Vance JE, Simmen T (2010) Ero1alpha
1333 requires oxidizing and normoxic conditions to localize to the mitochondria-associated membrane
1334 (MAM). Cell Stress Chaperones 15: 619-29
1335 Gnaiger E (2009) Capacity of oxidative phosphorylation in human skeletal muscle: new
1336 perspectives of mitochondrial physiology. Int J Biochem Cell Biol 41: 1837-45
1337 Goemans CV, Vertommen D, Agrebi R, Collet JF (2018) CnoX Is a Chaperedoxin: A Holdase that
1338 Protects Its Substrates from Irreversible Oxidation. Mol Cell 70: 614-627 e7
1339 Gorin Y, Ricono JM, Kim NH, Bhandari B, Choudhury GG, Abboud HE (2003) Nox4 mediates
1340 angiotensin II-induced activation of Akt/protein kinase B in mesangial cells. Am J Physiol Renal
1341 Physiol 285: F219-29
1342 Guerra C, Molinari M (2020) Thioredoxin-Related Transmembrane Proteins: TMX1 and Little
1343 Brothers TMX2, TMX3, TMX4 and TMX5. Cells 9
1344 Gutierrez T, Qi H, Yap MC, Tahbaz N, Milburn LA, Lucchinetti E, Lou PH, Zaugg M, LaPointe
1345 PG, Mercier P, Overduin M, Bischof H, Burgstaller S, Malli R, Ballanyi K, Shuai J, Simmen T (2020)
1346 The ER chaperone calnexin controls mitochondrial positioning and respiration. Sci Signal 13
1347 Hatzidaki E, Ntanovasilis DA, Papasotiriou I (2020) Novel antibody against TMX2 and its effects
1348 on breast cancer cells. Int J Biochem Mol Biol 11: 1-10
1349 Hoehne MN, Jacobs L, Lapacz KJ, Calabrese G, Murschall LM, Marker T, Kaul H, Trifunovic A,
1350 Morgan B, Fricker M, Belousov VV, Riemer J (2022) Spatial and temporal control of mitochondrial
1351 H(2) O(2) release in intact human cells. EMBO J 41: e109169

1352 Hu Y, Flockhart I, Vinayagam A, Bergwitz C, Berger B, Perrimon N, Mohr SE (2011) An
1353 integrative approach to ortholog prediction for disease-focused and other functional studies. BMC
1354 Bioinformatics 12: 357
1355 Jarvis RM, Hughes SM, Ledgerwood EC (2012) Peroxiredoxin 1 functions as a signal peroxidase
1356 to receive, transduce, and transmit peroxide signals in mammalian cells. Free Radic Biol Med 53:
1357 1522-30
1358 Jumper J, Evans R, Pritzel A, Green T, Figurnov M, Ronneberger O, Tunyasuvunakool K, Bates
1359 R, Zidek A, Potapenko A, Bridgland A, Meyer C, Kohl SAA, Ballard AJ, Cowie A, Romera-Paredes
1360 B, Nikolov S, Jain R, Adler J, Back T et al. (2021) Highly accurate protein structure prediction with
1361 AlphaFold. Nature 596: 583-589
1362 Klomsiri C, Nelson KJ, Bechtold E, Soito L, Johnson LC, Lowther WT, Ryu SE, King SB, Furdui
1363 CM, Poole LB (2010) Use of dimedone-based chemical probes for sulfenic acid detection evaluation of
1364 conditions affecting probe incorporation into redox-sensitive proteins. Methods Enzymol 473: 77-94
1365 Kraft AD, Johnson DA, Johnson JA (2004) Nuclear factor E2-related factor 2-dependent
1366 antioxidant response element activation by tert-butylhydroquinone and sulforaphane occurring
1367 preferentially in astrocytes conditions neurons against oxidative insult. J Neurosci 24: 1101-12
1368 Kreimendahl S, Schwichtenberg J, Gunnewig K, Brandherm L, Rassow J (2020) The selectivity
1369 filter of the mitochondrial protein import machinery. BMC Biol 18: 156
1370 Kucinska MK, Fedry J, Galli C, Morone D, Raimondi A, Solda T, Forster F, Molinari M (2023)
1371 TMX4-driven LINC complex disassembly and asymmetric autophagy of the nuclear envelope upon
1372 acute ER stress. Nat Commun 14: 3497
1373 Kwak C, Shin S, Park JS, Jung M, Nhung TTM, Kang MG, Lee C, Kwon TH, Park SK, Mun JY,
1374 Kim JS, Rhee HW (2020) Contact-ID, a tool for profiling organelle contact sites, reveals regulatory
1375 proteins of mitochondrial-associated membrane formation. Proc Natl Acad Sci U S A
1376 Lemieux H, Blier PU, Gnaiger E (2017) Remodeling pathway control of mitochondrial respiratory
1377 capacity by temperature in mouse heart: electron flow through the Q-junction in permeabilized fibers.
1378 Sci Rep 7: 2840
1379 Liedgens L, Zimmermann J, Waschenbach L, Geissel F, Laporte H, Gohlke H, Morgan B, Deponte
1380 M (2020) Quantitative assessment of the determinant structural differences between redox-active and
1381 inactive glutaredoxins. Nat Commun 11: 1725
1382 Lynes EM, Bui M, Yap MC, Benson MD, Schneider B, Ellgaard L, Berthiaume LG, Simmen T
1383 (2012) Palmitoylated TMX and calnexin target to the mitochondria-associated membrane. Embo J 31:
1384 457-70
1385 Marcogliese PC, Dutta D, Ray SS, Dang NDP, Zuo Z, Wang Y, Lu D, Fazal F, Ravenscroft TA,
1386 Chung H, Kanca O, Wan J, Douine ED, Network UD, Pena LDM, Yamamoto S, Nelson SF, Might M,
1387 Meyer KC, Yeo NC et al. (2022) Loss of IRF2BPL impairs neuronal maintenance through excess Wnt
1388 signaling. Sci Adv 8: eabl5613
1389 Marcogliese PC, Shashi V, Spillmann RC, Stong N, Rosenfeld JA, Koenig MK, Martinez-Agosto
1390 JA, Herzog M, Chen AH, Dickson PI, Lin HJ, Vera MU, Salamon N, Graham JM, Jr., Ortiz D, Infante
1391 E, Steyaert W, Dermaut B, Poppe B, Chung HL et al. (2018) IRF2BPL Is Associated with Neurological
1392 Phenotypes. Am J Hum Genet 103: 245-260
1393 Mast H, Holody CD, Lemieux H (2022) Fatty acid oxidation: a neglected factor in understanding
1394 the adjustment of mitochondrial function to cold temperatures. J Exp Biol 225
1395 Mognol GP, Gonzalez-Avalos E, Ghosh S, Spreafico R, Gudlur A, Rao A, Damoiseaux R, Hogan
1396 PG (2019) Targeting the NFAT:AP-1 transcriptional complex on DNA with a small-molecule inhibitor.
1397 Proc Natl Acad Sci U S A 116: 9959-9968
1398 Morgenstern M, Peikert CD, Lubbert P, Suppanz I, Klemm C, Alka O, Steiert C, Naumenko N,
1399 Schendzielorz A, Melchionda L, Muhlhauser WWD, Knapp B, Busch JD, Stiller SB, Dannenmaier S,

1400 Lindau C, Licheva M, Eickhorst C, Galbusera R, Zerbes RM et al. (2021) Quantitative high-confidence
1401 human mitochondrial proteome and its dynamics in cellular context. Cell Metab 33: 2464-2483 e18
1402 Nagarkar-Jaiswal S, DeLuca SZ, Lee PT, Lin WW, Pan H, Zuo Z, Lv J, Spradling AC, Bellen HJ
1403 (2015) A genetic toolkit for tagging intronic MiMIC containing genes. Elife 4
1404 Nelson KJ, Klomsiri C, Codreanu SG, Soito L, Liebler DC, Rogers LC, Daniel LW, Poole LB
1405 (2010) Use of dimedone-based chemical probes for sulfenic acid detection methods to visualize and
1406 identify labeled proteins. Methods Enzymol 473: 95-115
1407 Netto LE, Antunes F (2016) The Roles of Peroxiredoxin and Thioredoxin in Hydrogen Peroxide
1408 Sensing and in Signal Transduction. Mol Cells 39: 65-71
1409 Oguro A, Imaoka S (2019) Thioredoxin-related transmembrane protein 2 (TMX2) regulates the
1410 Ran protein gradient and importin-beta-dependent nuclear cargo transport. Sci Rep 9: 15296
1411 Olson HE, Jean-Marcais N, Yang E, Heron D, Tatton-Brown K, van der Zwaag PA, Bijlsma EK,
1412 Krock BL, Backer E, Kamsteeg EJ, Sinnema M, Reijnders MRF, Bearden D, Begtrup A, Telegrafi A,
1413 Lunsing RJ, Burglen L, Lesca G, Cho MT, Smith LA et al. (2018) A Recurrent De Novo PACS2
1414 Heterozygous Missense Variant Causes Neonatal-Onset Developmental Epileptic Encephalopathy,
1415 Facial Dysmorphism, and Cerebellar Dysgenesis. Am J Hum Genet 102: 995-1007
1416 Pannala VR, Dash RK (2015) Mechanistic characterization of the thioredoxin system in the
1417 removal of hydrogen peroxide. Free Radic Biol Med 78: 42-55
1418 Perea V, Cole C, Lebeau J, Dolina V, Baron KR, Madhavan A, Kelly JW, Grotjahn DA, Wiseman
1419 RL (2023) PERK signaling promotes mitochondrial elongation by remodeling membrane phosphatidic
1420 acid. EMBO J 42: e113908
1421 Poole LB, Klomsiri C, Knaggs SA, Furdui CM, Nelson KJ, Thomas MJ, Fetrow JS, Daniel LW,
1422 King SB (2007) Fluorescent and affinity-based tools to detect cysteine sulfenic acid formation in
1423 proteins. Bioconjug Chem 18: 2004-17
1424 Prasad M, Kaur J, Pawlak KJ, Bose M, Whittal RM, Bose HS (2015) Mitochondria-associated
1425 endoplasmic reticulum membrane (MAM) regulates steroidogenic activity via steroidogenic acute
1426 regulatory protein (StAR)-voltage-dependent anion channel 2 (VDAC2) interaction. J Biol Chem 290:
1427 2604-16
1428 Qiu ZP, Lin ZC, Hu A, Liu YB, Zeng WE, Zhao X, Shi XJ, Luo J, Song BL (2023)
1429 GRAMD1/ASTER-mediated cholesterol transport promotes Smoothened cholesterylation at the
1430 endoplasmic reticulum. EMBO J 42: e111513
1431 Rao RP, Scheffer L, Srideshikan SM, Parthibane V, Kosakowska-Cholody T, Masood MA,
1432 Nagashima K, Gudla P, Lockett S, Acharya U, Acharya JK (2014) Ceramide transfer protein deficiency
1433 compromises organelle function and leads to senescence in primary cells. PLoS One 9: e92142
1434 Rashed FB, Stoica AC, MacDonald D, El-Saidi H, Ricardo C, Bhatt B, Moore J, Diaz-Dussan D,
1435 Ramamonjisoa N, Mowery Y, Damaraju S, Fahlman R, Kumar P, Weinfeld M (2021) Identification of
1436 proteins and cellular pathways targeted by 2-nitroimidazole hypoxic cytotoxins. Redox Biol 41:
1437 101905
1438 Rath S, Sharma R, Gupta R, Ast T, Chan C, Durham TJ, Goodman RP, Grabarek Z, Haas ME,
1439 Hung WHW, Joshi PR, Jourdain AA, Kim SH, Kotrys AV, Lam SS, McCoy JG, Meisel JD, Miranda
1440 M, Panda A, Patgiri A et al. (2021) MitoCarta3.0: an updated mitochondrial proteome now with sub-
1441 organelle localization and pathway annotations. Nucleic Acids Res 49: D1541-D1547
1442 Raturi A, Gutierrez T, Ortiz-Sandoval C, Ruangkittisakul A, Herrera-Cruz MS, Rockley JP,
1443 Gesson K, Ourdev D, Lou PH, Lucchinetti E, Tahbaz N, Zaugg M, Baksh S, Ballanyi K, Simmen T
1444 (2016) TMX1 determines cancer cell metabolism as a thiol-based modulator of ER-mitochondria Ca2+
1445 flux. J Cell Biol 214: 433-44

1446 Reina S, Pittala MGG, Guarino F, Messina A, De Pinto V, Foti S, Saletti R (2020) Cysteine
1447 Oxidations in Mitochondrial Membrane Proteins: The Case of VDAC Isoforms in Mammals. Front
1448 Cell Dev Biol 8: 397
1449 Rhee SG (2016) Overview on Peroxiredoxin. Mol Cells 39: 1-5
1450 Selak MA, Armour SM, MacKenzie ED, Boulahbel H, Watson DG, Mansfield KD, Pan Y, Simon
1451 MC, Thompson CB, Gottlieb E (2005) Succinate links TCA cycle dysfunction to oncogenesis by
1452 inhibiting HIF-alpha prolyl hydroxylase. Cancer Cell 7: 77-85
1453 Sharma LK, Fang H, Liu J, Vartak R, Deng J, Bai Y (2011) Mitochondrial respiratory complex I
1454 dysfunction promotes tumorigenesis through ROS alteration and AKT activation. Hum Mol Genet 20:
1455 4605-16
1456 Shoshan-Barmatz V, Krelin Y, Shteinfer-Kuzmine A (2018) VDAC1 functions in Ca(2+)
1457 homeostasis and cell life and death in health and disease. Cell Calcium 69: 81-100
1458 Shutt T, Geoffrion M, Milne R, McBride HM (2012) The intracellular redox state is a core
1459 determinant of mitochondrial fusion. EMBO Rep 13: 909-15
1460 Simmen T, Herrera-Cruz MS (2018) Plastic mitochondria-endoplasmic reticulum (ER) contacts
1461 use chaperones and tethers to mould their structure and signaling. Curr Opin Cell Biol 53: 61-69
1462 Staudacher V, Trujillo M, Diederichs T, Dick TP, Radi R, Morgan B, Deponte M (2018) Redox-
1463 sensitive GFP fusions for monitoring the catalytic mechanism and inactivation of peroxiredoxins in
1464 living cells. Redox Biol 14: 549-556
1465 Thaher O, Wolf C, Dey PN, Pouya A, Wullner V, Tenzer S, Methner A (2018) The thiol switch
1466 C684 in Mitofusin-2 mediates redox-induced alterations of mitochondrial shape and respiration.
1467 Neurochem Int 117: 167-173
1468 Theurey P, Tubbs E, Vial G, Jacquemetton J, Bendridi N, Chauvin MA, Alam MR, Le Romancer
1469 M, Vidal H, Rieusset J (2016) Mitochondria-associated endoplasmic reticulum membranes allow
1470 adaptation of mitochondrial metabolism to glucose availability in the liver. J Mol Cell Biol
1471 Thi My Nhung T, Phuoc Long N, Diem Nghi T, Suh Y, Hoang Anh N, Jung CW, Minh Triet H,
1472 Jung M, Woo Y, Yoo J, Noh S, Kim SJ, Lee SB, Park S, Thomas G, Simmen T, Mun J, Rhee HW,
1473 Kwon SW, Park SK (2023) Genome-wide kinase-MAM interactome screening reveals the role of
1474 CK2A1 in MAM Ca(2+) dynamics linked to DEE66. Proc Natl Acad Sci U S A 120: e2303402120
1475 Tubbs E, Rieusset J (2016) Study of Endoplasmic Reticulum and Mitochondria Interactions by In
1476 Situ Proximity Ligation Assay in Fixed Cells. J Vis Exp
1477 Tubbs E, Theurey P, Vial G, Bendridi N, Bravard A, Chauvin MA, Ji-Cao J, Zoulim F, Bartosch
1478 B, Ovize M, Vidal H, Rieusset J (2014) Mitochondria-associated endoplasmic reticulum membrane
1479 (MAM) integrity is required for insulin signaling and is implicated in hepatic insulin resistance.
1480 Diabetes 63: 3279-94
1481 Vance JE (2015) Phospholipid synthesis and transport in mammalian cells. Traffic 16: 1-18
1482 Vance JE (2020) Inter-organelle membrane contact sites: implications for lipid metabolism. Biol
1483 Direct 15: 24
1484 Vandervore LV, Schot R, Milanese C, Smits DJ, Kasteleijn E, Fry AE, Pilz DT, Brock S, Borklu-
1485 Yucel E, Post M, Bahi-Buisson N, Sanchez-Soler MJ, van Slegtenhorst M, Keren B, Afenjar A, Coury
1486 SA, Tan WH, Oegema R, de Vries LS, Fawcett KA et al. (2019) TMX2 Is a Crucial Regulator of
1487 Cellular Redox State, and Its Dysfunction Causes Severe Brain Developmental Abnormalities. Am J
1488 Hum Genet 105: 1126-1147
1489 Wieckowski MR, Giorgi C, Lebiedzinska M, Duszynski J, Pinton P (2009) Isolation of
1490 mitochondria-associated membranes and mitochondria from animal tissues and cells. Nat Protoc 4:
1491 1582-90
1492 Wood ZA, Poole LB, Karplus PA (2003) Peroxiredoxin evolution and the regulation of hydrogen
1493 peroxide signaling. Science 300: 650-3

1494 Yeo HK, Park TH, Kim HY, Jang H, Lee J, Hwang GS, Ryu SE, Park SH, Song HK, Ban HS,
1495 Yoon HJ, Lee BI (2021) Phospholipid transfer function of PTPIP51 at mitochondria-associated ER
1496 membranes. EMBO Rep 22: e51323
1497 Yoast RE, Emrich SM, Zhang X, Xin P, Arige V, Pathak T, Benson JC, Johnson MT, Abdelnaby
1498 AE, Lakomski N, Hempel N, Han JM, Dupont G, Yule DI, Sneyd J, Trebak M (2021) The
1499 Mitochondrial Ca(2+) uniporter is a central regulator of interorganellar Ca(2+) transfer and NFAT
1500 activation. J Biol Chem 297: 101174
1501 Yoboue ED, Sitia R, Simmen T (2018) Redox crosstalk at endoplasmic reticulum (ER) membrane
1502 contact sites (MCS) uses toxic waste to deliver messages. Cell Death Dis 9: 331
1503 Zardini Buzatto A, Sarkar I, van Drunen Littel-van den Hurk S, Li L (2020) Comprehensive
1504 Lipidomic and Metabolomic Analysis for Studying Metabolic Changes in Lung Tissue Induced by a
1505 Vaccine against Respiratory Syncytial Virus. ACS Infect Dis 6: 2130-2142
1506 Zhang M, Mileykovskaya E, Dowhan W (2002) Gluing the respiratory chain together. Cardiolipin
1507 is required for supercomplex formation in the inner mitochondrial membrane. J Biol Chem 277: 43553-
1508 6
1509 Zimmermann J, Oestreicher J, Geissel F, Deponte M, Morgan B (2021) An intracellular assay for
1510 activity screening and characterization of glutathione-dependent oxidoreductases. Free Radic Biol Med
1511 172: 340-349
1512

Figure 1 *(Chen et al, 2023)*

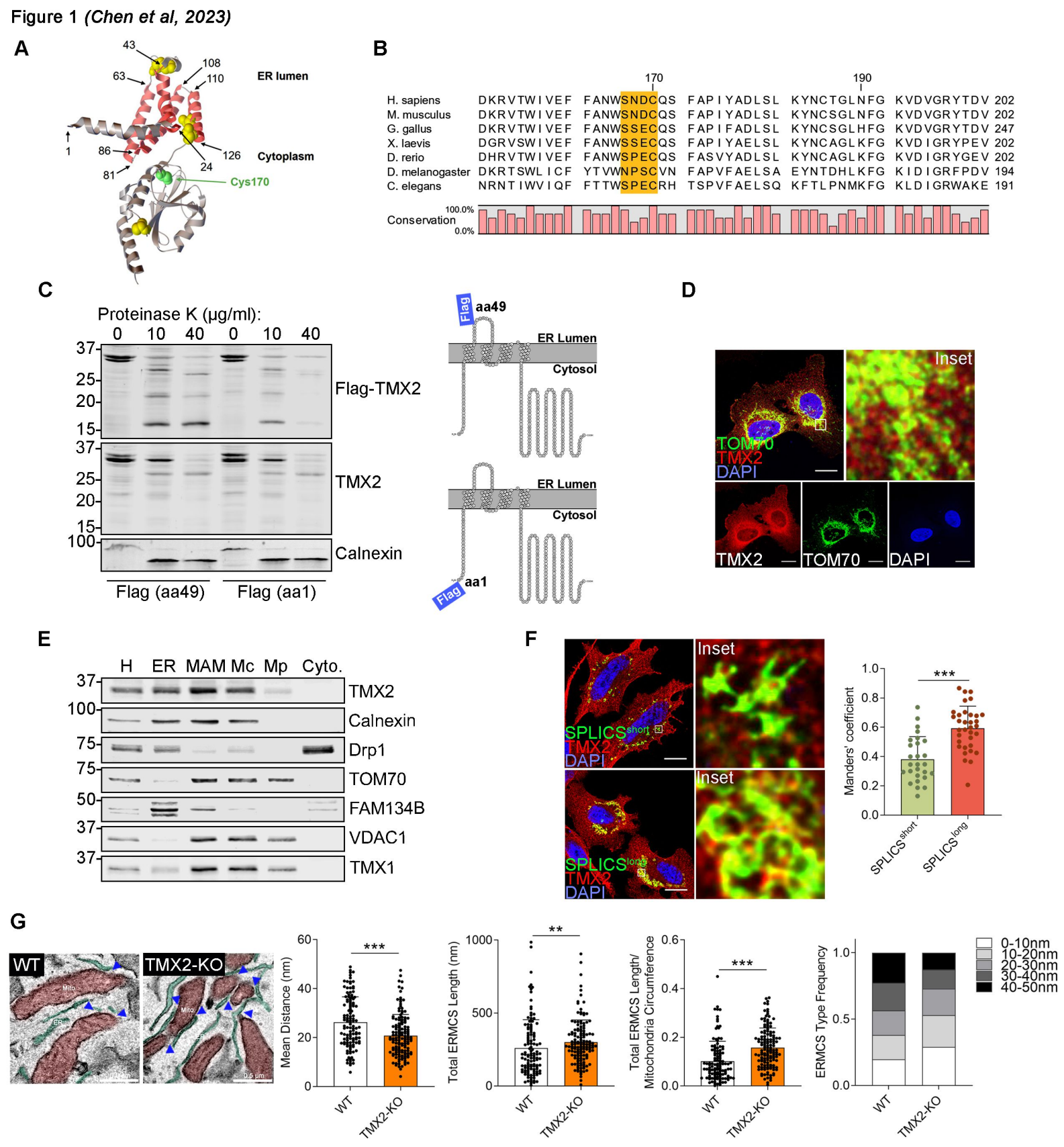

Figure 2 *(Chen et al, 2023)*

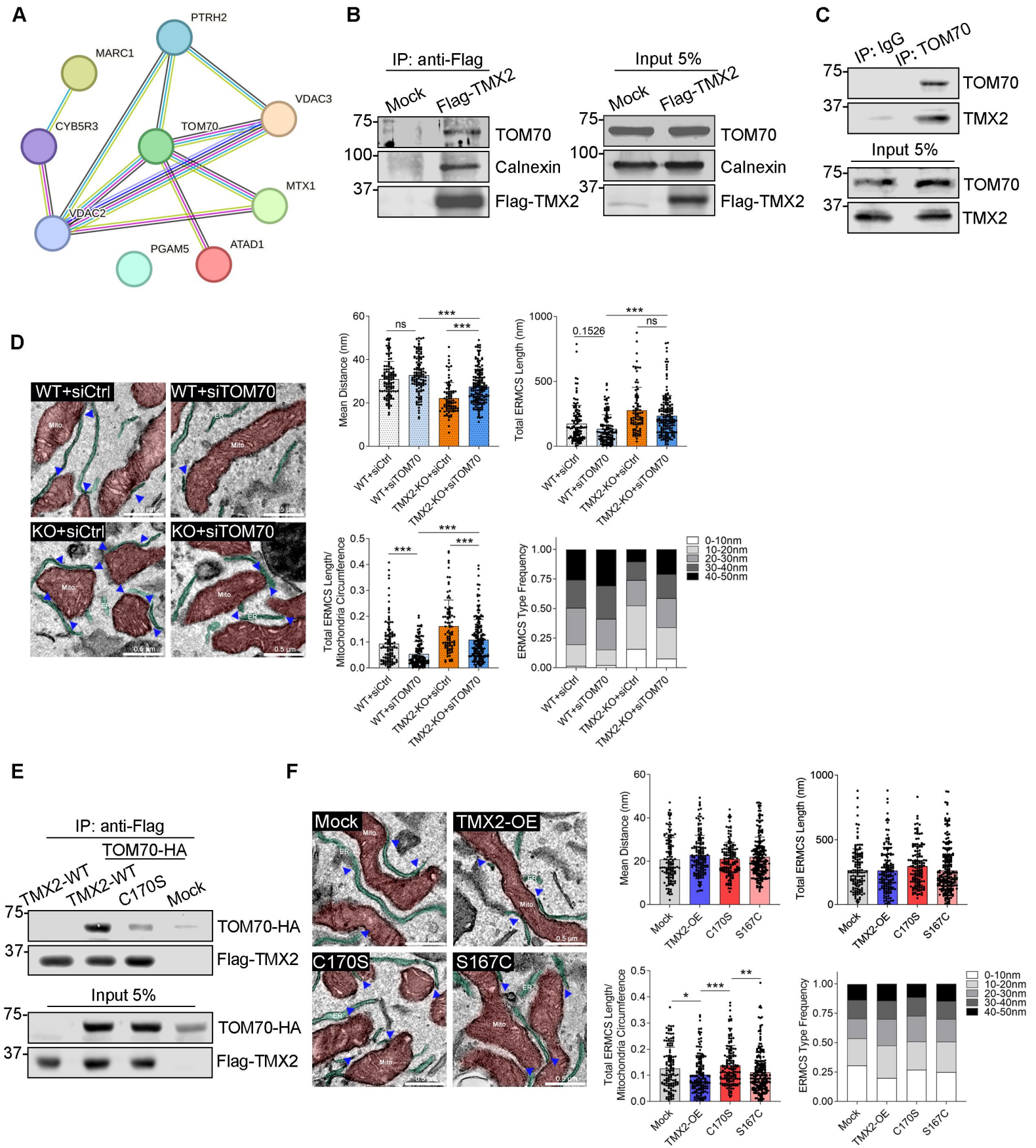

Figure 3 *(Chen et al, 2023)*

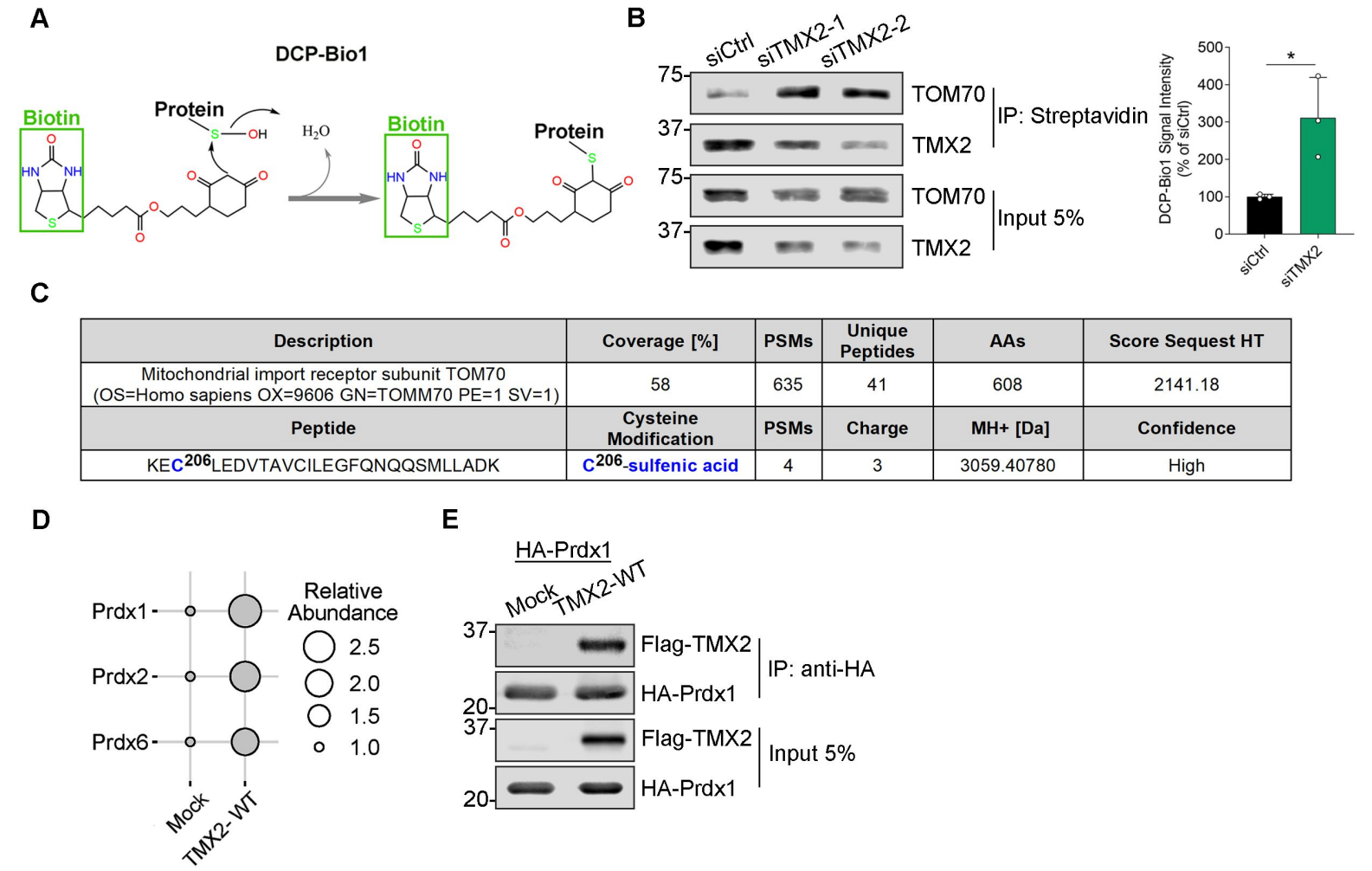

C

Description	Coverage [%]	PSMs	Unique Peptides	AAs	Score Sequest HT
Mitochondrial import receptor subunit TOM70 (OS=Homo sapiens OX=9606 GN=TOMM70 PE=1 SV=1)	58	635	41	608	2141.18
Peptide	**Cysteine Modification**	**PSMs**	**Charge**	**MH+ [Da]**	**Confidence**
KEC^{206}LEDVTAVCILEGFQNQQSMLLADK	C^{206}-sulfenic acid	4	3	3059.40780	High

Figure 4 *(Chen et al, 2023)*

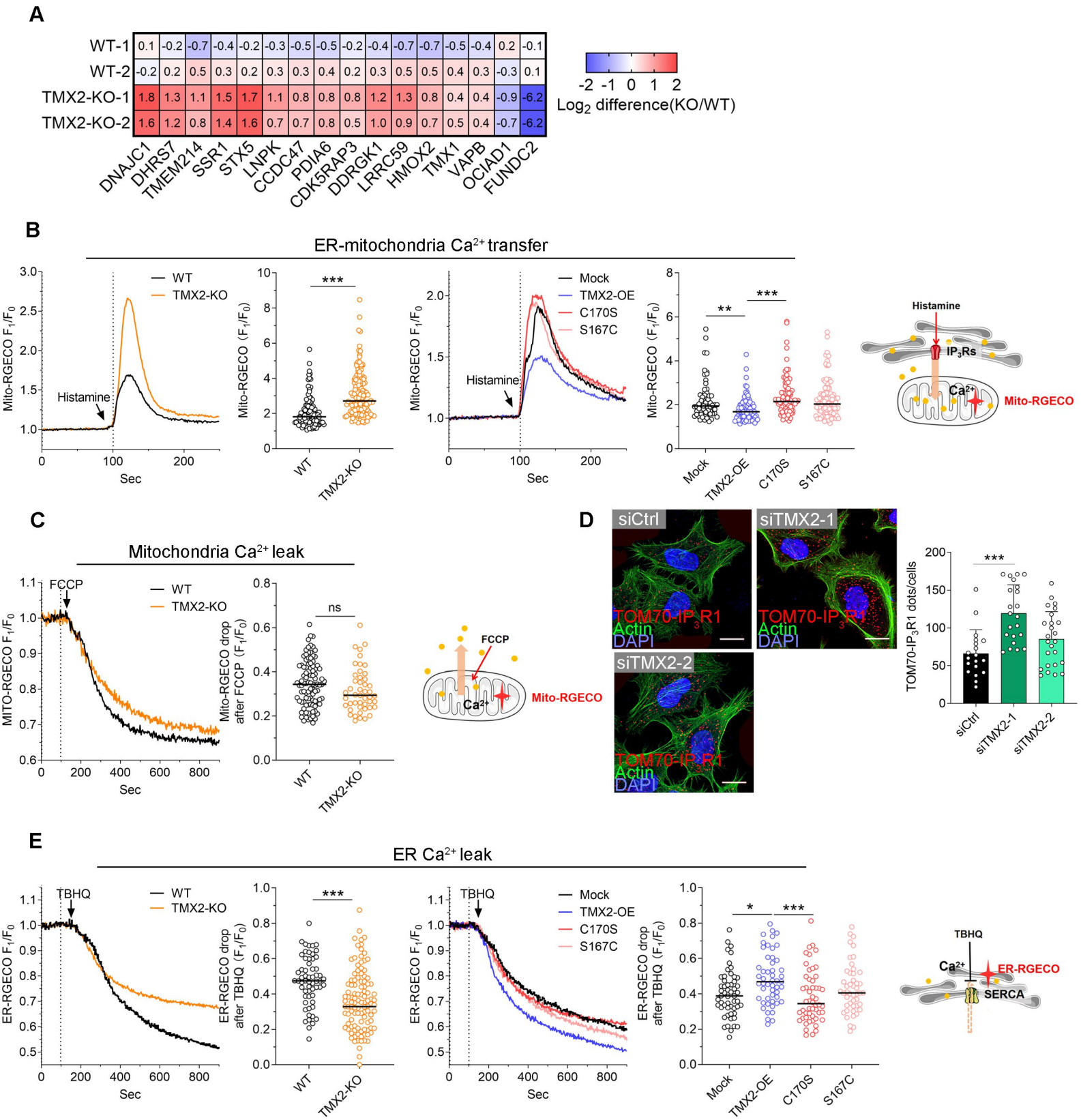

Figure 5 *(Chen et al, 2023)*

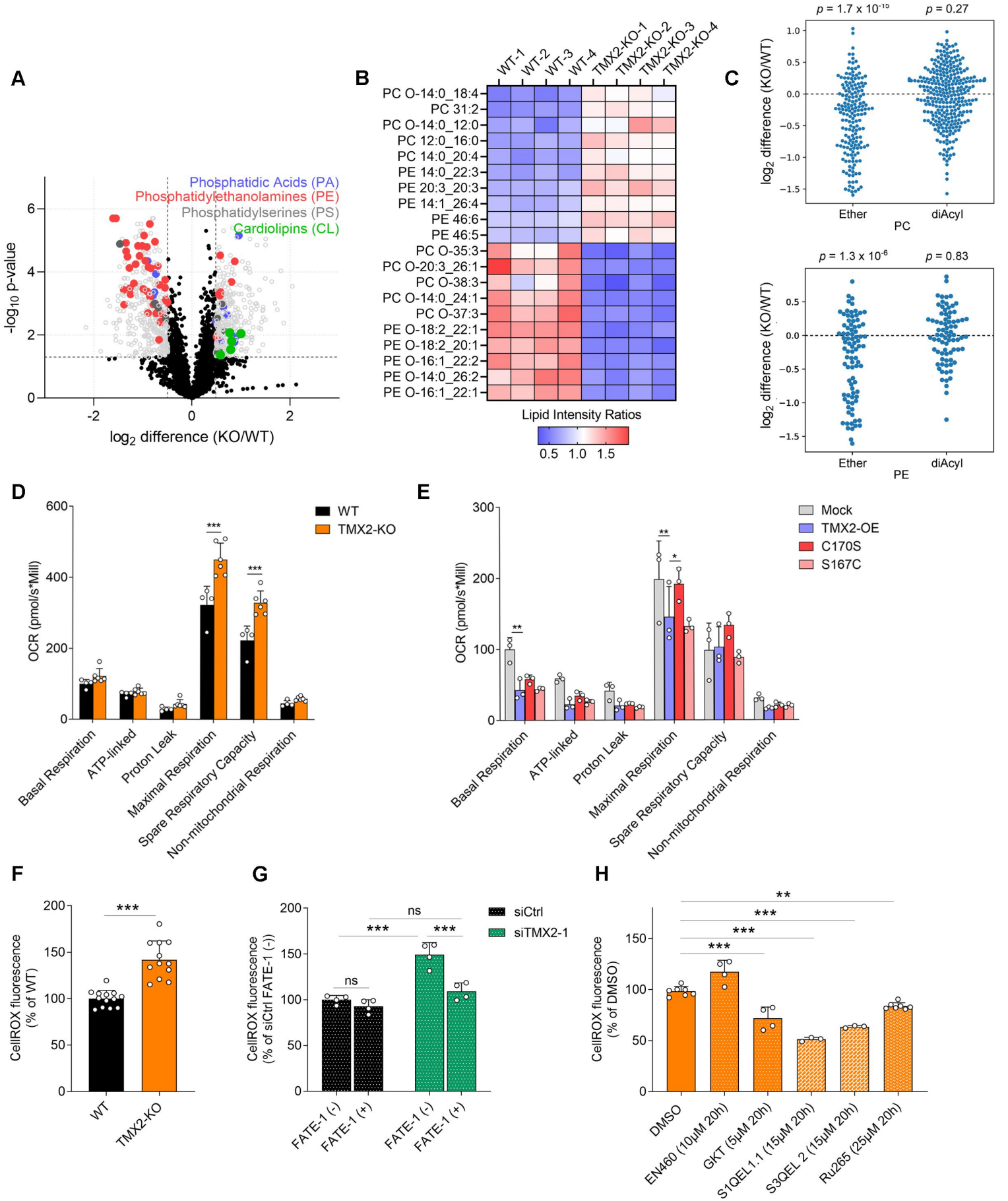

Figure 6 *(Chen et al, 2023)*

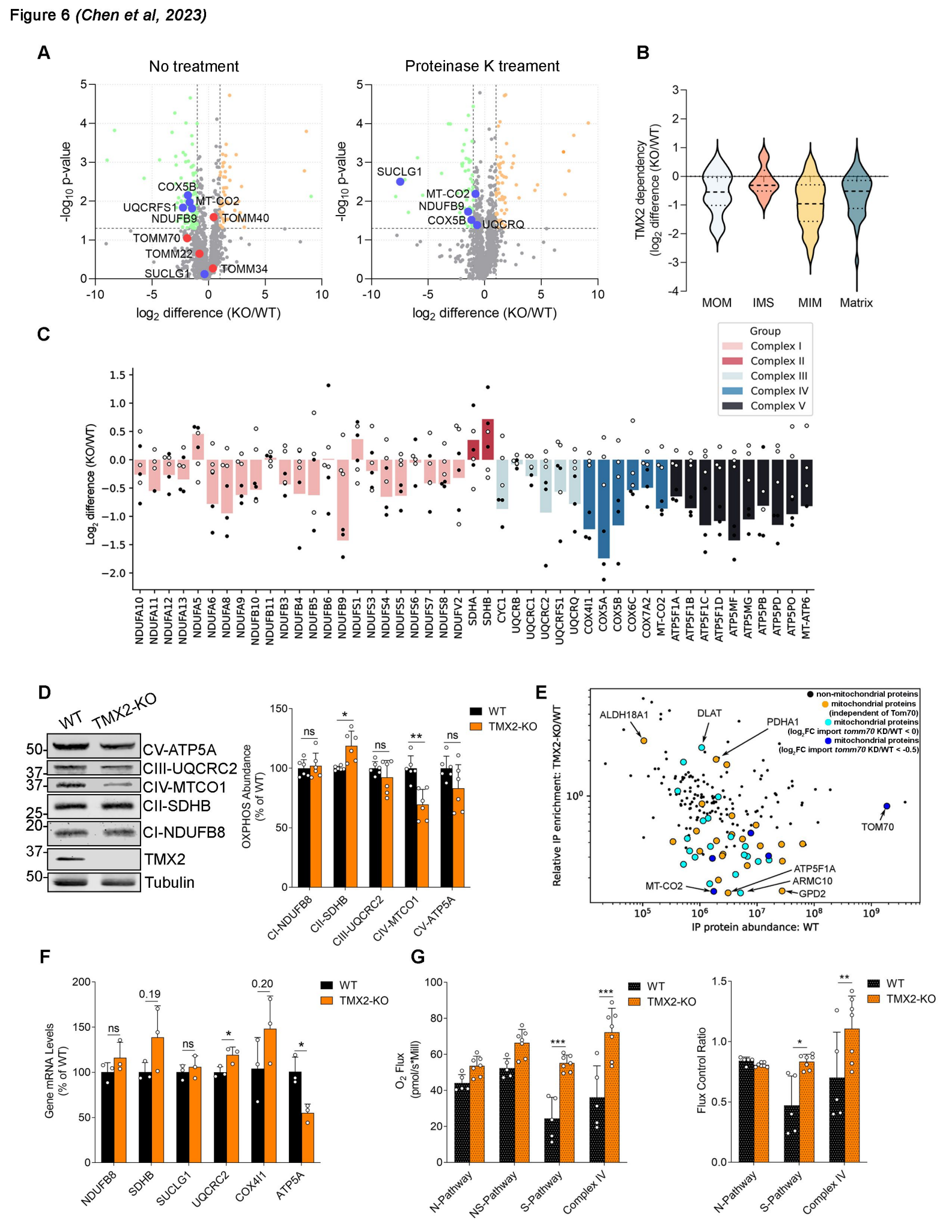

Figure 7 *(Chen et al, 2023)*

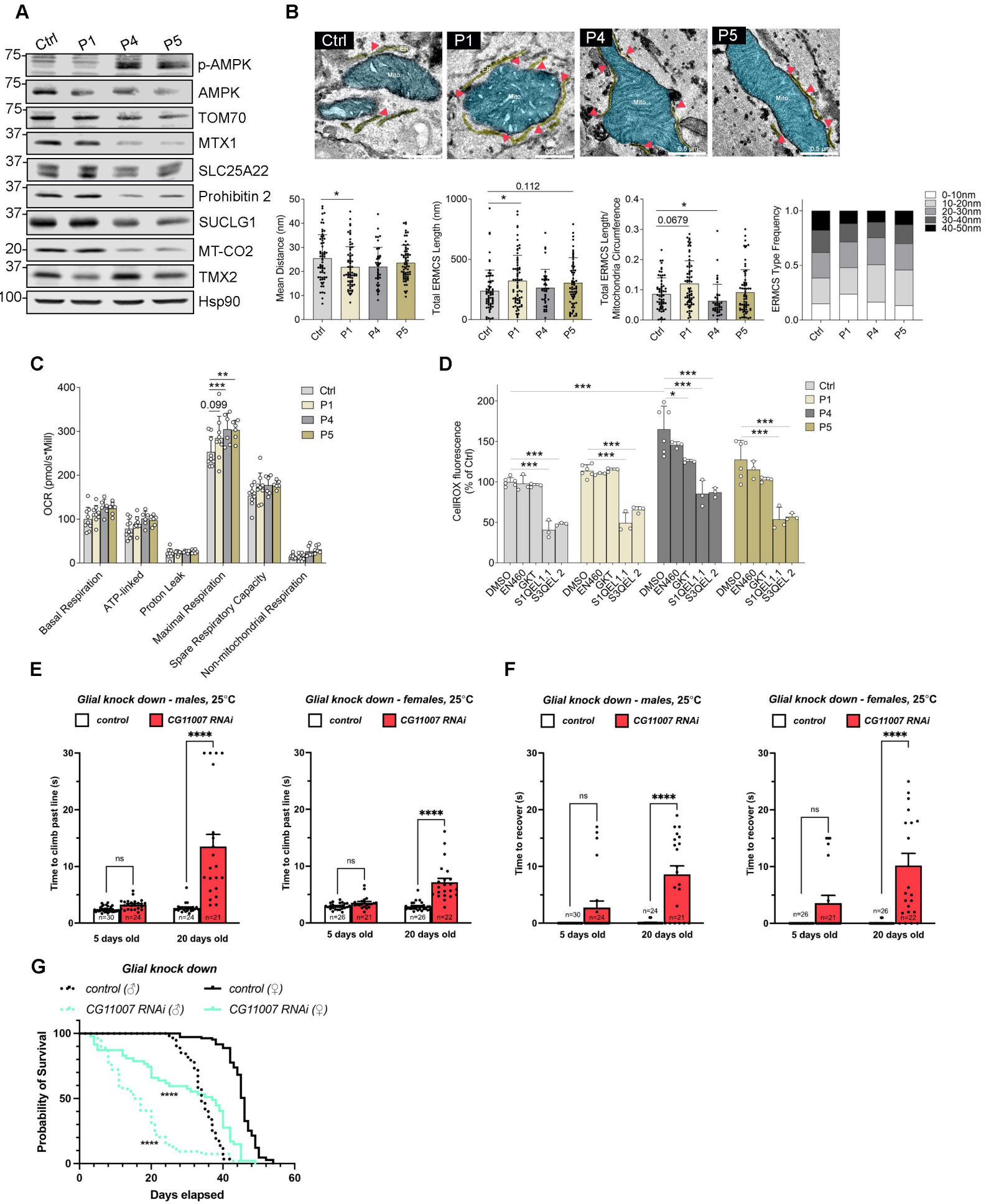

Figure S1 *(Chen et al, 2023)*

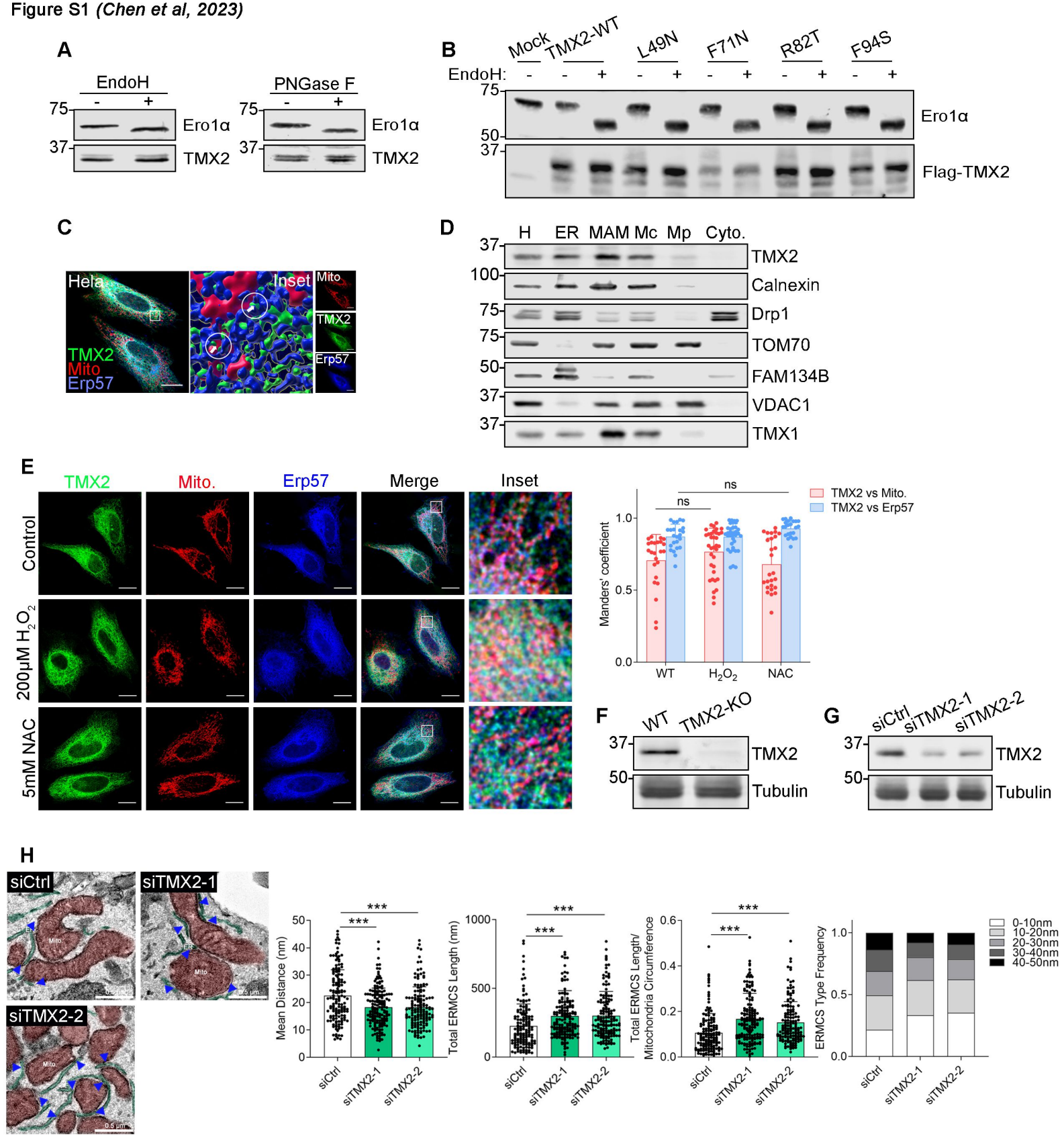

Figure S2 *(Chen et al, 2023)*

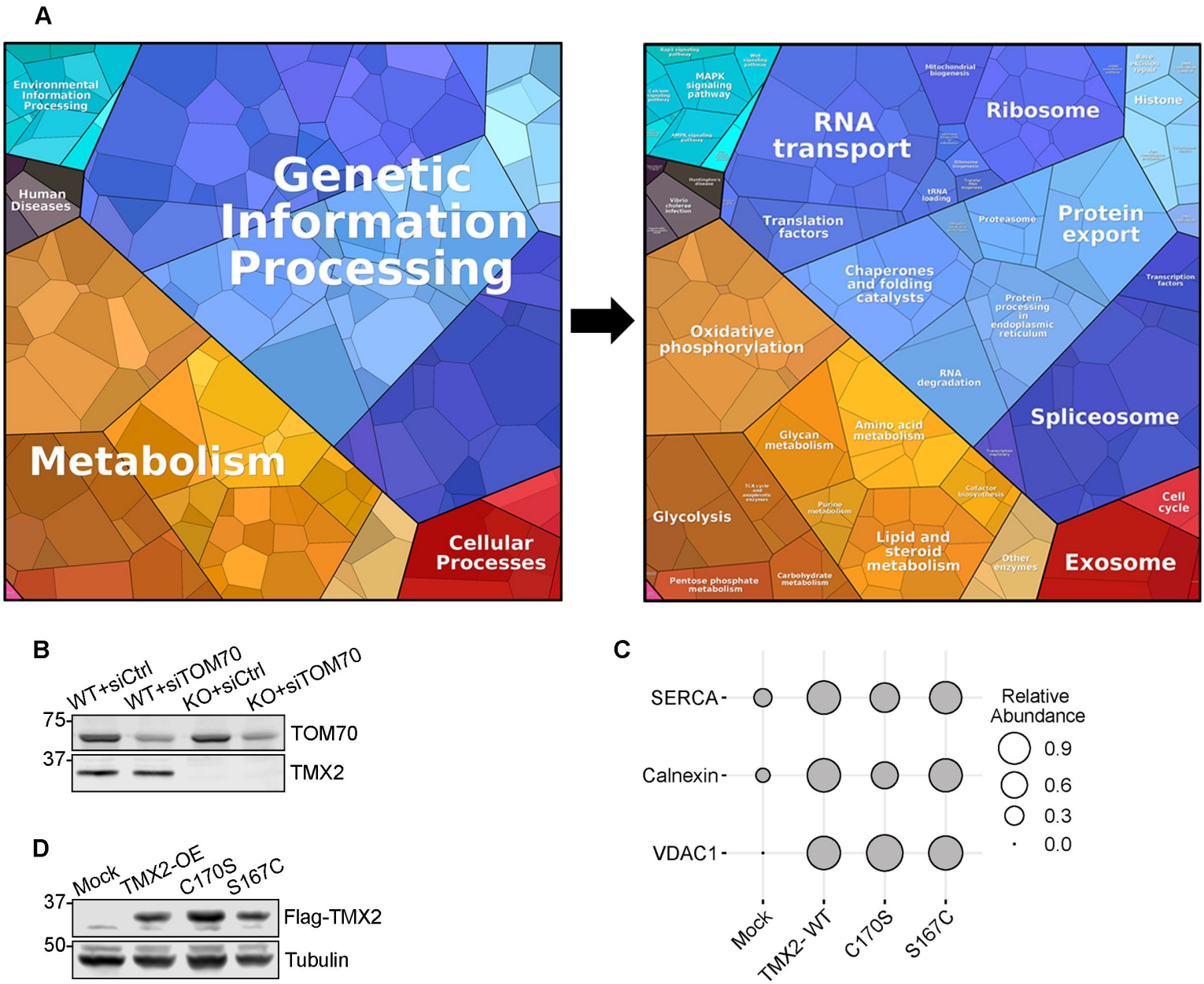

Figure S3 *(Chen et al, 2023)*

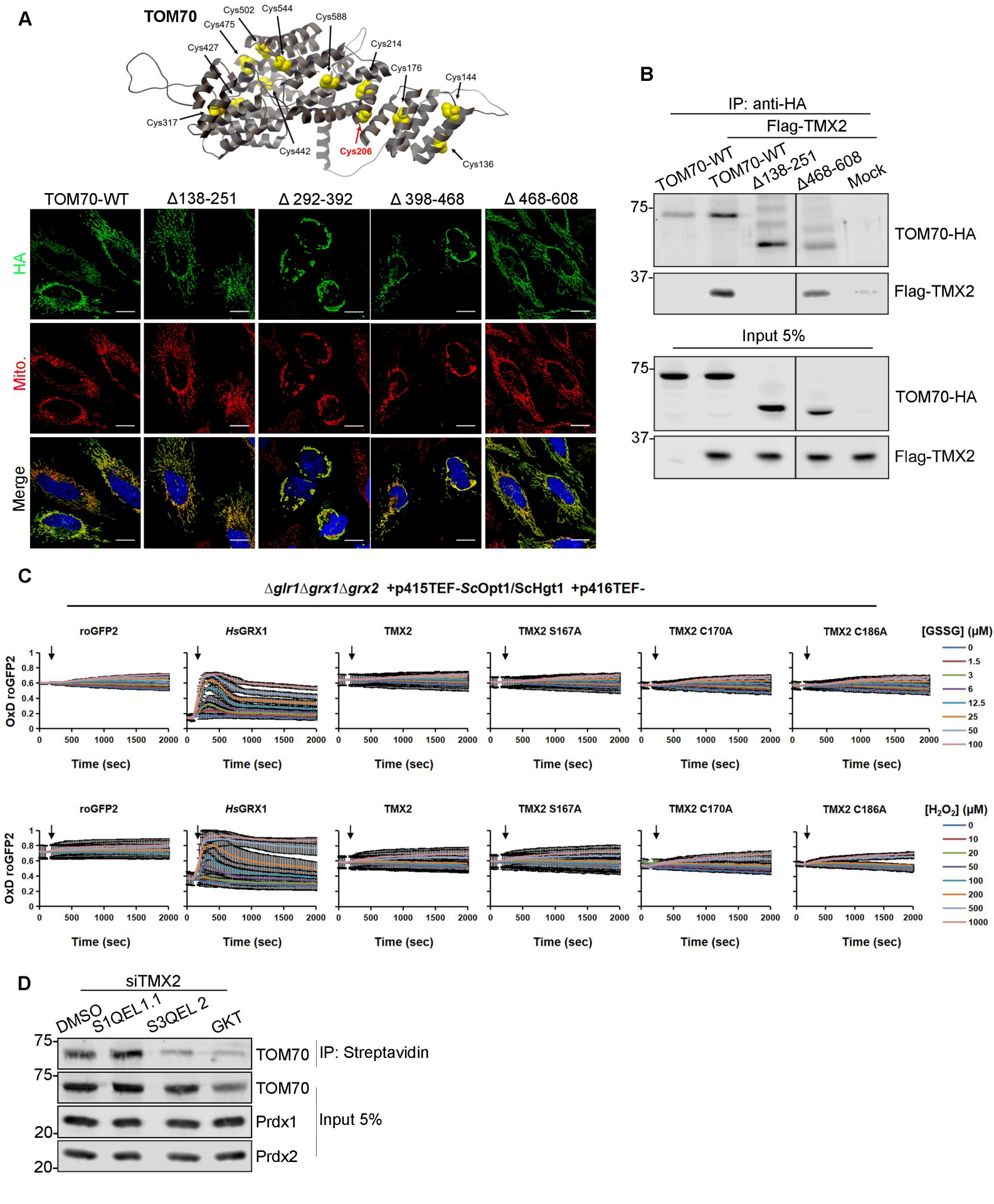

Figure S4 *(Chen et al, 2023)*

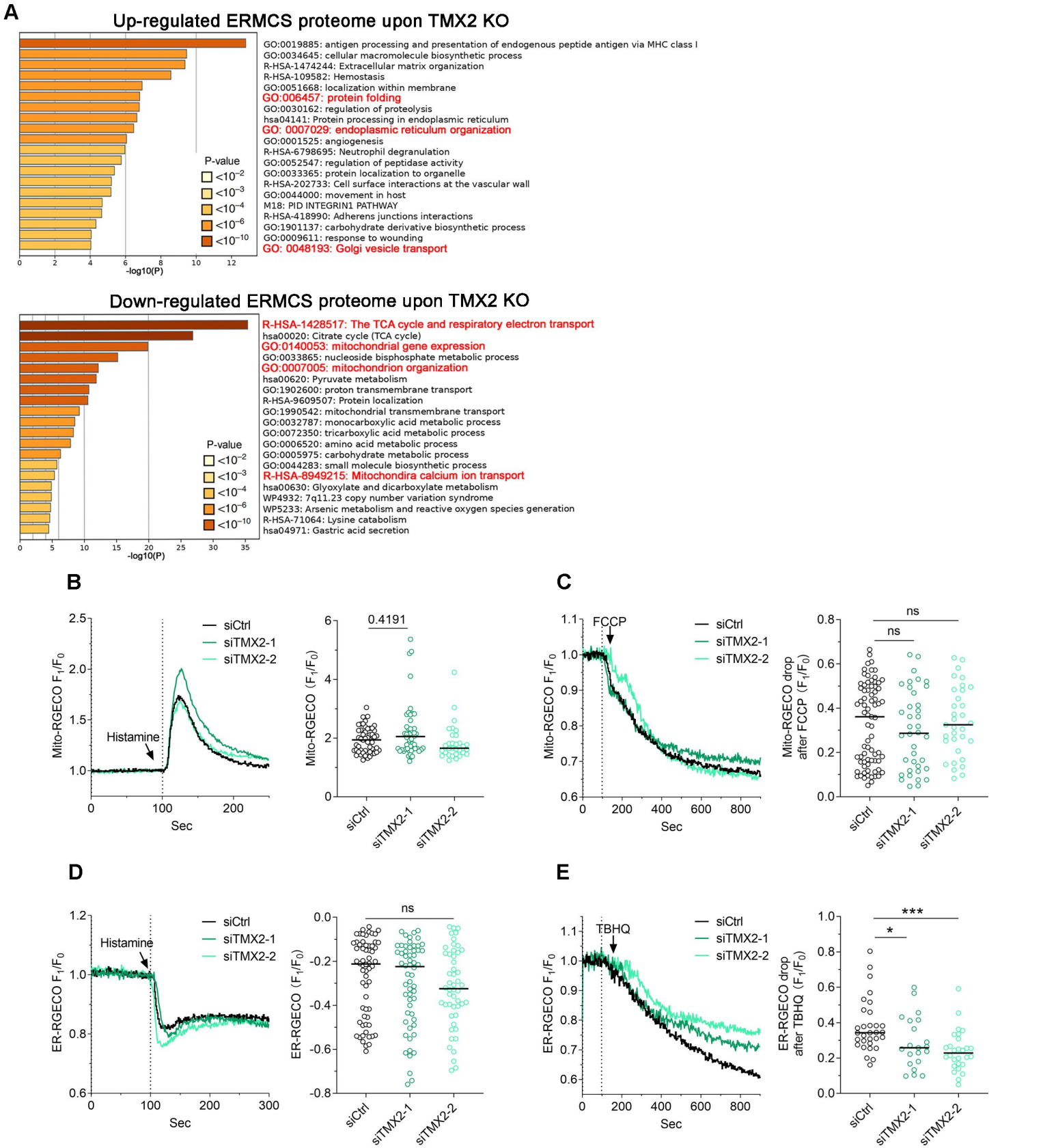

Figure S5 *(Chen et al, 2023)*

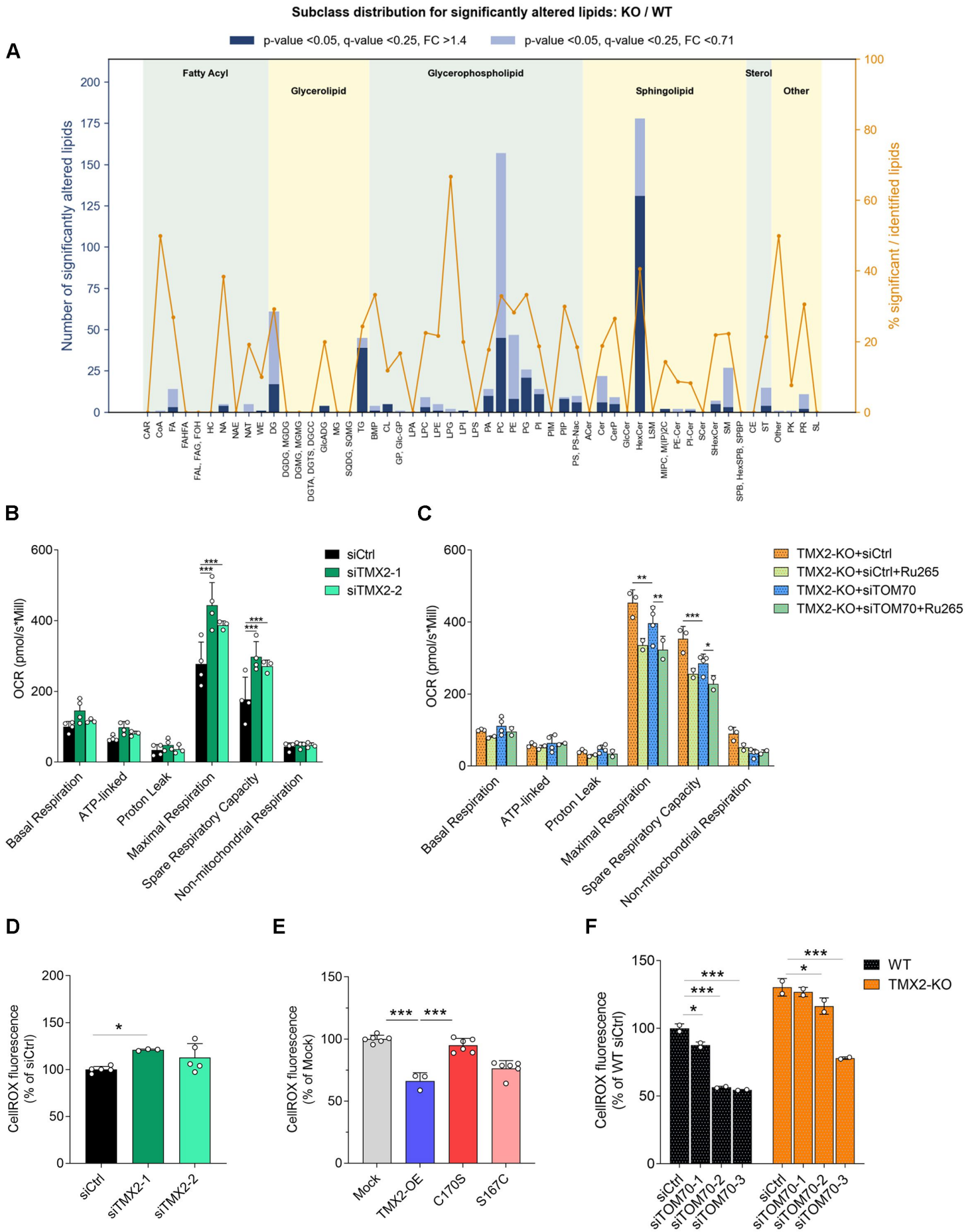

Figure S6 *(Chen et al, 2023)*

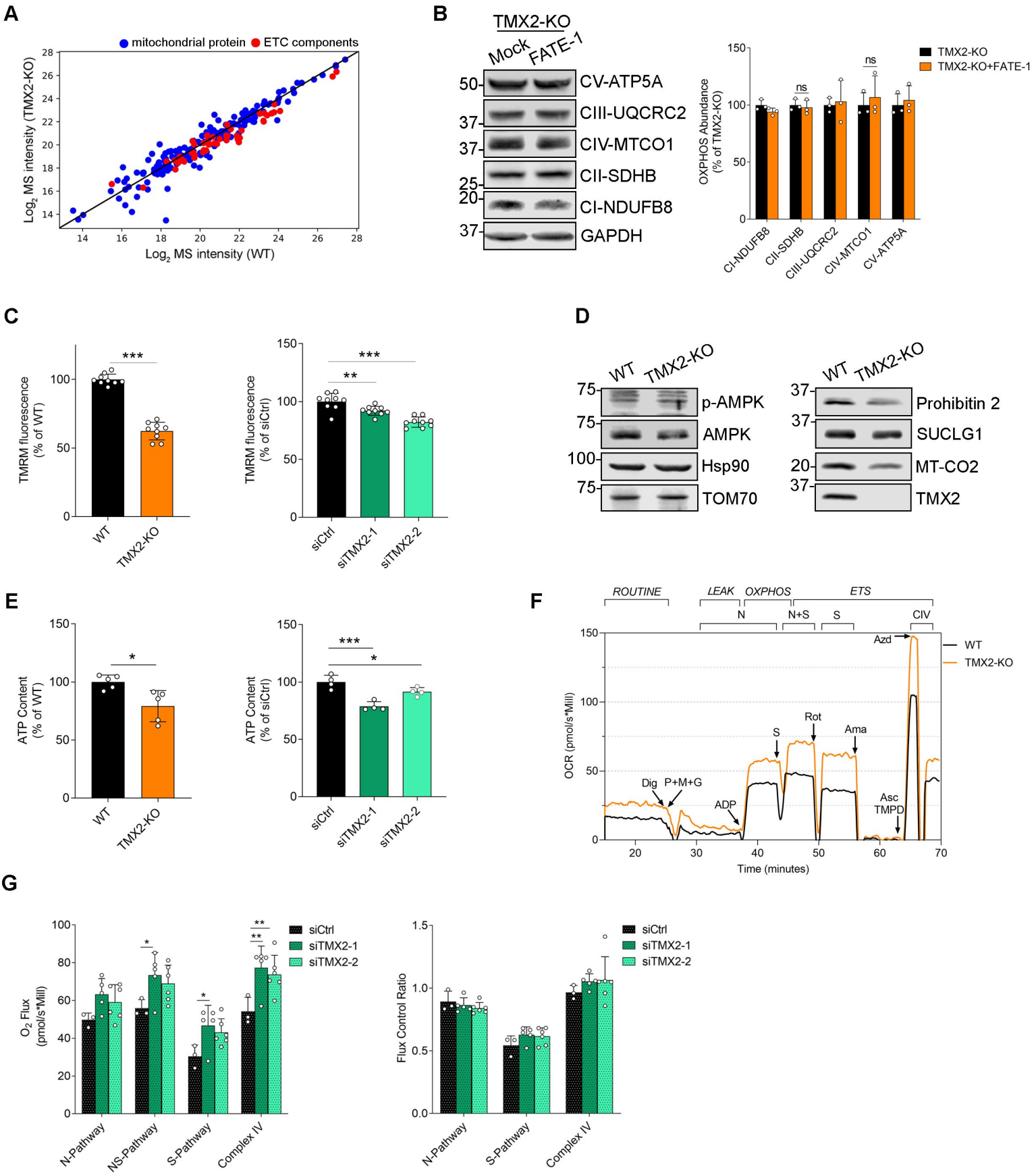

Figure S7 *(Chen et al, 2023)*

A

Affected Individuals	P1	P4	P5
Ancestry	Dutch	Puerto Rican	Puerto Rican
cDNA alteration	c.164A>C; c.391dup	c.166G>C homozygote	c.166G>C homozygote
Protein alteration	p.Asp55Al; p.Leu131Profs*6	p.Gly56Arg	p.Gly56Arg
Gender	male	male	female
Head size (OFC)	primary microcephaly (-3 SD at birth)	borderline microcephaly (NA at birth; -2 SD current)	microcephaly (NA at birth; -3 SD current)
Neurological impairment	no developmental milestones	CP, no speech or ambulation	CP, no speech or ambulation
Survival/age at last examination	deceased at 2 weeks	28 years	25 years
Epilepsy	generalized, apnea, status epilepticus	focal seizures	myoclonic-absence, GTC
MRI	polymicrogyria	progressive brain atrophy	progressive brain atrophy
Brain autopsy	unlayered polymicrogyria and complete corticol disorganization	NA	NA

B

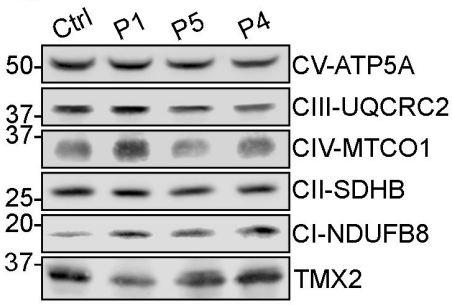

C

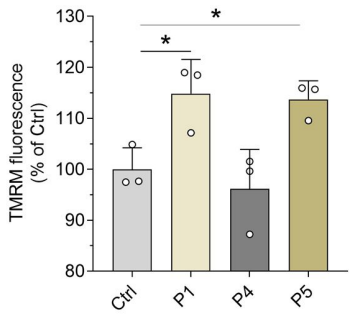

D

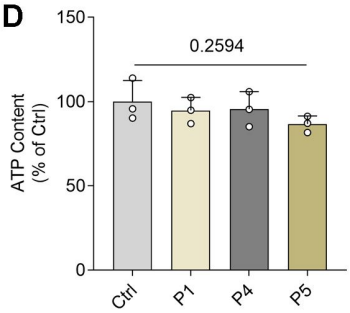

E

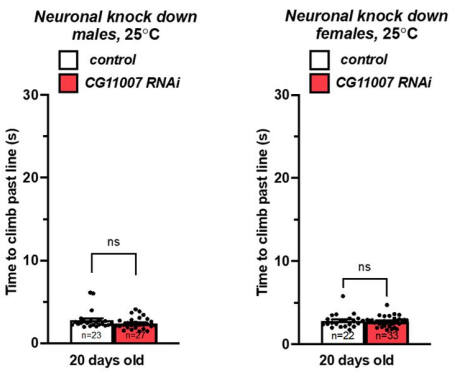

F

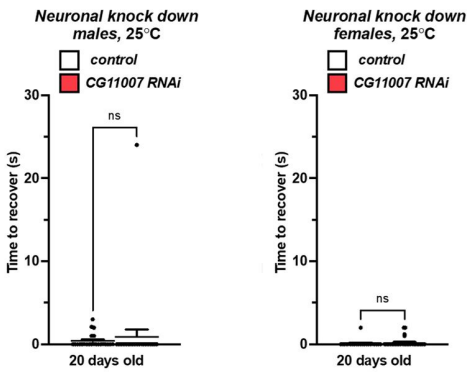

G

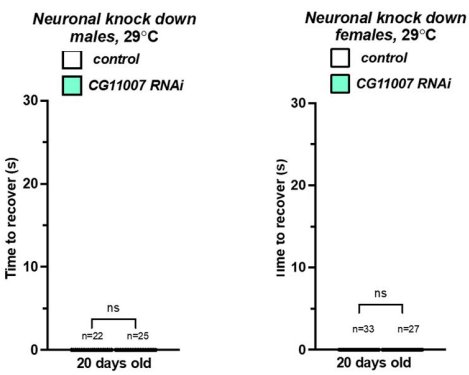

H

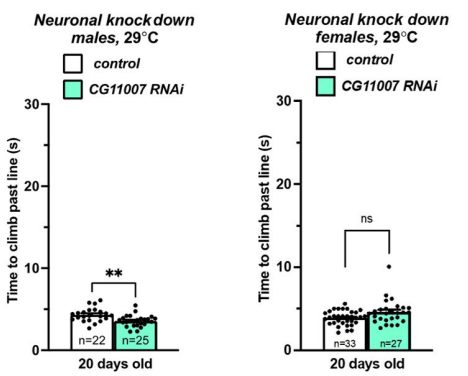

I

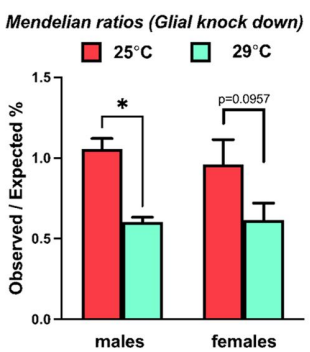

J

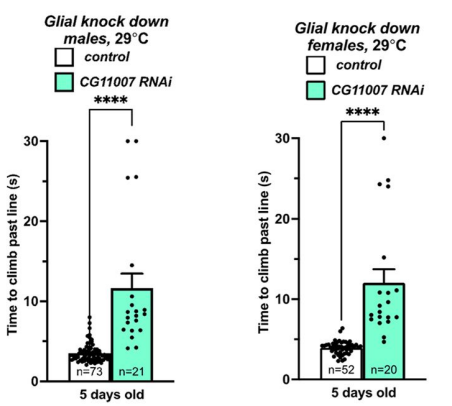

K

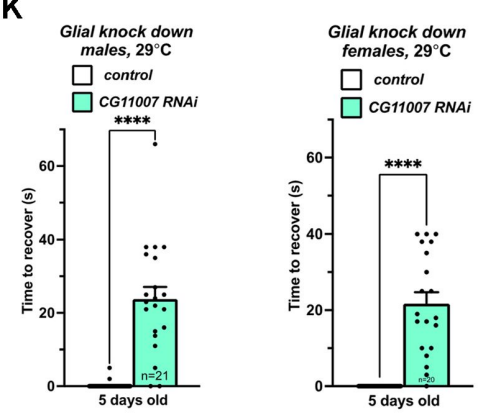

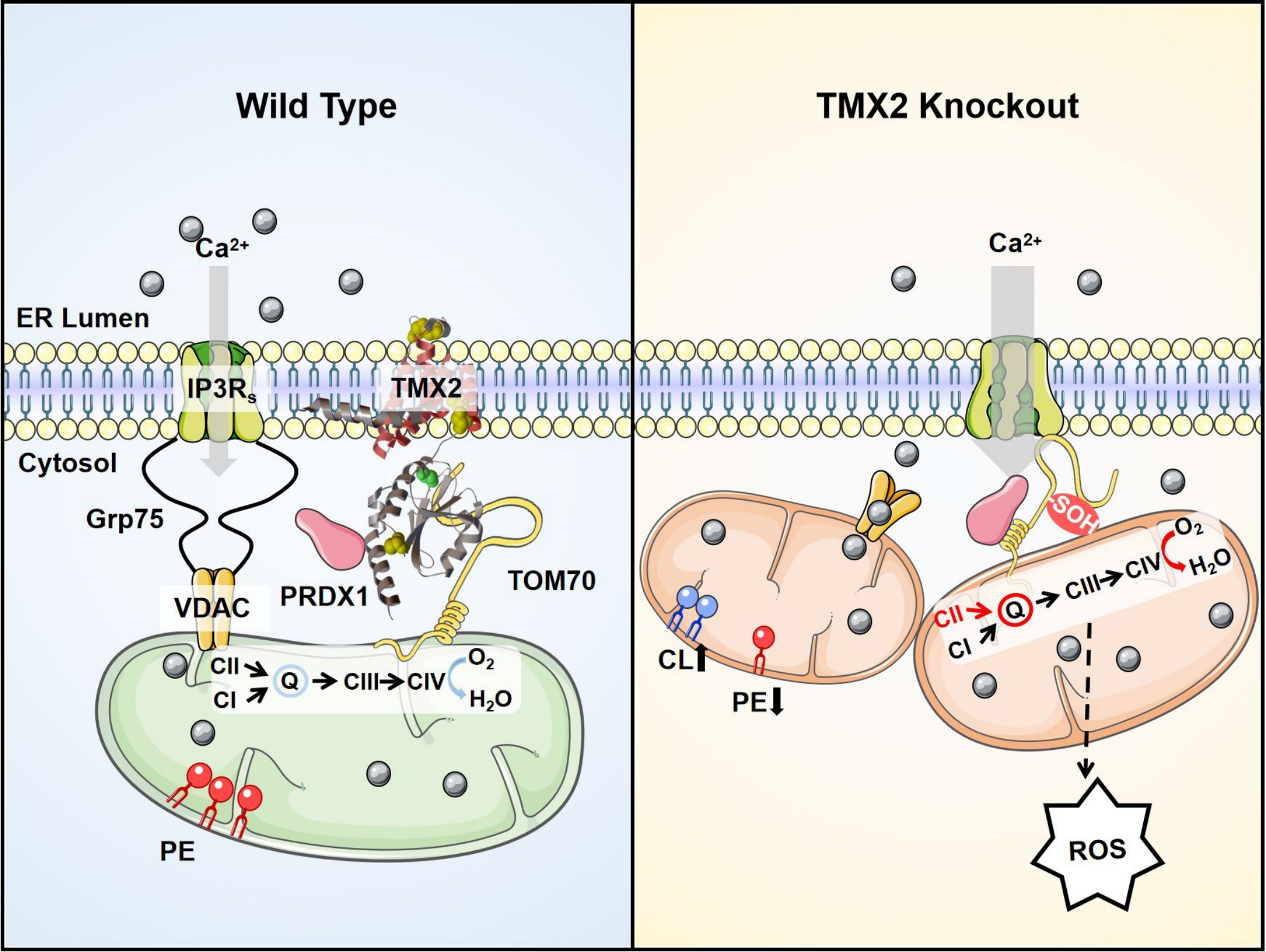
Wild Type
Ca2+
ER Lumen
IP3Rs
TMX2
Cytosol
Grp75
VDAC
PRDX1
TOM70
CII
CI
Q
CIII
CIV
O2
H2O
PE
TMX2 Knockout
Ca2+
SOH
CL
PE
CII
CI
Q
CIII
CIV
O2
H2O
ROS